http://www.journals.elsevier.com/
journal-of-energy-chemistry/

Supporting IrO_2 and $IrRuO_x$ nanoparticles on TiO_2 and Nb-doped TiO_2 nanotubes as electrocatalysts for the oxygen evolution reaction

Radostina V. Genova-Koleva , Francisco Alcaide ,
Garbiñe Álvarez , Pere L. Cabot , Hans-Jürgen Grande ,
María V. Martínez-Huerta , Oscar Miguel

PII: S2095-4956(19)30075-0
DOI: https://doi.org/10.1016/j.jechem.2019.03.008
Reference: JECHEM 795

To appear in: *Journal of Energy Chemistry*

Received date: 15 January 2019
Revised date: 4 March 2019
Accepted date: 5 March 2019

Please cite this article as: Radostina V. Genova-Koleva , Francisco Alcaide , Garbiñe Álvarez , Pere L. Cabot , Hans-Jürgen Grande , María V. Martínez-Huerta , Oscar Miguel , Supporting IrO_2 and $IrRuO_x$ nanoparticles on TiO_2 and Nb-doped TiO_2 nanotubes as electrocatalysts for the oxygen evolution reaction, *Journal of Energy Chemistry* (2019), doi: https://doi.org/10.1016/j.jechem.2019.03.008

Highlights

- (Nb-)TiO_2 nanotubes have been used as support of IrO_2 and $IrRuO_x$ catalysts
- The Nb-doped TiO_2 nanotubes have significant specific surface area of 260 m^2 g^{-1}
- XPS analysis shows an electronic effect of Nb on Ti and Ir in IrO_2/Nb-TNT catalyst
- IrO_2/Nb-TNT catalyst shows higher number of active sites, dispersion and stability
- The best OER performance in acid media is presented by the IrO_2/Nb-TNT catalyst

Supporting IrO_2 and $IrRuO_x$ nanoparticles on TiO_2 and Nb-doped TiO_2 nanotubes as electrocatalysts for the oxygen evolution reaction

Radostina V. Genova-Koleva[b], Francisco Alcaide[a,*], Garbiñe Álvarez[a], Pere L. Cabot[b], Hans-Jürgen Grande[a], María V. Martínez-Huerta[c], Oscar Miguel[a]

[a] *CIDETEC, Pº Miramón, 196, 20009 San Sebastián, Spain*

[b] *Laboratory of Electrochemistry of Materials and the Environment, Dep. of Materials Science and Physical Chemistry, Universitat de Barcelona, Martí i Franqués 1-11, 08028 Barcelona, Spain*

[c] *Instituto de Catálisis y Petroleoquímica, CSIC, C/ Marie Curie, 2. 28049 Madrid, Spain*

*Corresponding author. Tel: +34 943 309 022, Fax: +34 943 309 136, E-mail address: falcaide@cidetec.es (F. Alcaide).

Abstract

IrO_2 and $IrRuO_x$ (Ir:Ru 60:40 at%), supported by 50 wt% onto titania nanotubes (TNTs) and (3 at% Nb) Nb-doped titania nanotubes (Nb-TNTs), as electrocatalysts for the oxygen evolution reaction (OER), were synthesized and characterized by means of structural, surface analytical and electrochemical techniques. Nb doping of titania significantly increased the surface area of the support from 145 (TNTs) to 260 m^2 g^{-1} (Nb-TNTs), which was significantly higher than those of the Nb-doped titania supports previously reported in the literature. The surface analytical techniques showed good dispersion of the catalysts onto the supports. The X-ray photoelectron spectroscopy analyses showed that Nb was mainly in the form of Nb(IV) species, the suitable form to behave as a donor introducing free electrons to the conduction band of titania. The redox transitions of the cyclic voltammograms, in agreement with the XPS results, were found to be reversible. Despite the supported materials presented bigger crystallite sizes than the unsupported ones, the total number of active sites of the former was also higher due to their better catalyst dispersion. Considering the outer and the total charges of the cyclic voltammograms in the range 0.1–1.4 V, stability and electrode potentials at given current densities, the preferred catalyst was IrO_2 supported on the Nb-TNTs. The electrode potentials corresponding to given current densities were between the smallest ones given in the literature despite the small oxide loading used in this work and its Nb doping, thus making the Nb-TNTs-supported IrO_2 catalyst a promising candidate for the OER. The good dispersion of IrO_2, high specific surface area of the Nb-doped supports, accessibility of the electroactive centers, increased stability due to Nb doping and electron donor properties of the Nb(IV) oxide species were considered the main reasons for its good performance.

Keywords: Nb-doped TiO_2 nanotubes; IrO_2 catalyst; $IrRuO_x$ catalyst; Oxygen evolution reaction; PEMWE

1. Introduction

It is out of doubt that the energy resources of the mankind have to change from fossil fuels to renewable ones to limit the climatic change. Hydrogen appears to be the clean fuel of the future and water splitting is considered a suitable form to obtain this source of sustainable carbon-neutral energy. For this purpose, electrocatalysts leading to low overpotentials for both, hydrogen and oxygen evolution, are essential for an efficient and low-energy consumption water splitting. Noble metal-based electrocatalysts have generally shown their superior performance for this application [1]. However, they are scarce, expensive and do not always exhibit good durability. On the other hand, the oxygen evolution reaction (OER) appears to be the bottleneck because of its sluggish reaction kinetics. For this reaction, high performances have been recorded using non-noble metals in strongly alkaline solutions [1–5], but they do not appear to have sufficient chemical stability when applied in acidic electrolytes. It is worth to note that strong alkaline and acidic electrolytes are corrosive and pollutant to the environment. For this reason, the electrocatalyst modification to be applied in neutral water, where its catalytic behavior is worse, is foreseen. In the meanwhile, the use of devices such as polymer exchange membrane water electrolyzers (PEMWEs) appears to be a good alternative. The electrolyte is a hydrated proton exchange membrane, which is acidic, but compact, with no losses to the environment, with successful application for example in polymer electrolyte fuel cells, whose reactions are still dependent on Pt-based catalysts.

High corrosion resistance materials are essential for the OER in the anodes of the PEMWEs, where they can be oxidized due to the high anodic potentials required. This makes anodic materials one of the main challenges for its development [6,7]. Developing new catalysts that are more active and/or depositing the catalysts onto suitable supports are typical procedures allowing improving the catalyst performance. It has been shown that the supports are important not only to increase the active surface area of the catalysts, but to integrate the catalyst-support feature in order to improve the charge transfer efficiency between them [4]. The stability under the operating conditions of the cell is one of the main requirements that catalyst supports should meet. With the exception of advanced carbon supports such as carbon nanobowls, which appeared to be very stable in acidic media as supports for ultrafine Ir nanocrystals [8], carbons can suffer oxidation during the OER. For this reason, one of the main targets is the research of new non-carbon supports for anodes in PEMWEs [9].

The electrocatalysts for the OER are generally unsupported due to the high potentials applied to the anode, in which conventional supports such as carbon-based ones can be easily oxidized. Ru and RuO_2 appear to be the best electrocatalysts for the OER [10]. However, they are not sufficiently stable. The use of Ir black under the operating conditions of the anode leads to its surface oxidation to iridium oxides [11]. IrO_2 is much more stable and, in addition, it is a very active anodic electrocatalyst. It has been widely used for membrane-electrode assembly (MEA) preparation, optimization and evaluation [12–16]. Typical loads of the electrocatalyst are 2–4 mg cm^{-2} and decreasing this amount would be welcome. Some attempts to stabilize the more active, but less stable RuO_2 by either, supporting it or forming mixed oxides with the more stable IrO_2 have been done [17–19]. In order to attempt higher electrocatalytic performance, IrO_2 has been prepared together with other oxides such as Ta_2O_5 [18,19] or SnO_2, either forming mixed oxides or using SnO_2 as support [6,20]. No other effect than IrO_2 dilution in the case of mixed oxide formation has been mentioned. Mixed oxides containing up to 20 mol% SnO_2 only led to a small change in the active area. However, significant improvement in the anodic kinetics of water electrolysis at 80 and 130 °C for IrO_2 supported on Sb-doped SnO_2 and tin pyrophosphate was reported.

Titania supports for IrO_2 have also been studied [21,22]. TiO_2 offers very high stability and resistance under the anode conditions, but it has a low conductivity [9,21,23]. Using commercial TiO_2 powders, with specific surface areas from 10 to 90 m^2 g^{-1}, and IrO_2/TiO_2 catalysts with 60 wt% IrO_2, it was found that the lower the specific surface area of the support the higher was the electrochemical activity of the catalyst [21]. This was explained by the formation of a conductive IrO_2 film on the surface of the non-conductive supports, which was able to cover the low specific surface area of the TiO_2 powder and therefore, to approach that of unsupported IrO_2. The conductivity of TiO_2 could be significantly improved by doping with donor ions such as Nb, in which the donor energy level is formed in the band gap and the electron can be excited to the conduction band [24]. A corrosion-resistant nanosized $Nb_{0.05}Ti_{0.95}O_2$ support with high surface area of 83 m^2 g^{-1} was prepared by a sol-gel process [25]. The catalyst with an IrO_2 loading of 26 wt% exhibited the best mass normalized activity (loadings in the range 15–100 wt%), which was explained by the uniform supporting of the IrO_2 nanoparticles on the surface, thus providing conductive channels to reduce the grain boundary resistance. Recently, mesoporous Nb-doped TiO_2 supports with Nb contents in the range 5–20 at% and specific surface areas up to 146.5 m^2 g^{-1} were prepared by the modified evaporation-induced self-assembly method, which induced grain refinement and uniform dispersion [22]. The OER activity increased with Nb content, explained by the Nb-doping induced enhancement of the specific surface area and surface activity of transferring charge and species with the help of the Nb(IV)/Nb(V) redox couple, which was superior to that of pristine titania-supported IrO_2 and unsupported IrO_2. In addition, accelerated durability tests showed very good stability when using the Nb-doped TiO_2-supports, which was much better than that of unsupported IrO_2.

In this work, titania and Nb-doped titania nanotube, not previously tested in the literature as supports for the IrO_2 and $IrRuO_x$ were synthesized. Because of the use of the nanotubes, higher specific surface areas than those previously reported for the titania supports, was expected. IrO_2 and $IrRuO_x$ catalysts were synthesized and deposited on the supports by 50 wt%. The unsupported and the supported catalysts were characterized by means of X-ray diffraction, transmision and high resolution transmission electron micrsocopy, energy-dispersive X-ray spectroscopy, X-ray photoelectron spectroscopy and their catalytic performance and stability was studied by means of cyclic and linear sweep voltammetry in a three-electrode cell using small catalyst loadings of 35 μg cm^{-2}, which was much lower than those typically used in PEMWEs. The corresponding results have been compared to previous ones reported in the literature.

2. Experimental

2.1 Synthesis of supports and electrocatalysts

The titania nanotubes (TNTs) and the Nb-doped titania nanotubes with 3 at% Nb (Nb-TNTs) to be used as supports of the catalysts were synthesized following the modified hydrothermal method described previously [23,26]. TiO_2 and Nb-doped TiO_2 (3 at%) were first obtained by means of the sol-gel technique. Titanium (IV) n-butoxide (98%, Alfa Aesar) and niobium (V) ethoxide (99,999%, Alfa Aesar), the latter used as 0.20 mol dm^{-3} solution in absolute ethanol, were mixed in absolute ethanol media in appropriate ratio (3 at% Nb toward Ti). Then, hydrochloric acid (37%, Scharlau) at a molar ratio HCl:Ti+Nb 1:1 and ultrapure water (resistivity greater than 18.2 MΩ cm, Millipore Corp.) at a molar ratio H_2O:Ti+Nb 50:1 were added and the mixture was vigorously stirred at room temperature for 1 h. At the end, the gellification of the sol was achieved by adding 1.0 mol dm^{-3} ammonium carbonate (aqueous solution) [27,28]. The final product was filtered, washed and dried at 60 ºC for 10 h and after that annealed at 350 °C in air atmosphere [29]. After the synthesis, 1 g of TiO_2 or of Nb-doped TiO_2 was dispersed in 10 mol dm^{-3} NaOH contained in a Teflon vessel, which was sonicated for 2 h and then heated for 72 h at 130 °C. Afterwards, the layered sodium titanates ($Na_2Ti_xO_{2x+1}$) thus obtained were treated with 0.1 mol dm^{-3} HCl leading to the formation of protonated tubular titanates ($H_2Ti_xO_{2x+1}$), which were rinsed with ultrapure water. The product was then dried at 60 °C for 10 h. In addition, protonated titanates were calcined at 350 ºC for 2.5 h to obtain pristine TNTs and Nb-TNTs supports when needed.

The supported (50 wt%) IrO_2 and $IrRuO_x$ catalysts were synthesized by hydrolysis of their chlorides in alkaline media, following the procedure previously indicated in the literature [14,30,31]. On one hand, the required amounts of $IrCl_3{\cdot}xH_2O$ (99.9%, Alfa Aesar) and protonated titanates were dispersed in 150 mL of ultrapure water (150 mL water per each 100 mg of the material) and sonicated for 30 min. The pH was adjusted to 12 with 1.0 mol dm^{-3} NaOH and the mixture was stirred at 80 ºC for 2 h. At the end the pH was adjusted to 8 with 0.10 mol dm^{-3} HNO_3 (ultrapure, Scharlab) followed by additional 30 min stirring. The product was filtered and washed with ultrapure water, dried for 12 h at 80 ºC and finally calcined at 350 ºC for 2.5 h to obtain IrO_2 supported on the TNTs and the Nb-TNTs. On the other hand, $IrCl_3{\cdot}xH_2O$ (99.9%, Alfa Aesar) and $RuCl_3{\cdot}xH_2O$ (99.9%, Alfa Aesar) with Ir:Ru atomic ratio of 60:40 were used to prepare the supported $IrRuO_x$ catalyst in the same form as for supported IrO_2. Unsupported IrO_2 and $IrRuO_x$ blacks were prepared following the same procedure and calcined at 350 ºC for 2.5 h. The resulting materials will then be named as unsupported IrO_2 and $IrRuO_x$, IrO_2/TNT, IrO_2/Nb-TNT, $IrRuO_x$/TNT and $IrRuO_x$/Nb-TNT.

2.2 Physicochemical characterization

The nitrogen adsorption/desorption isotherms of the supports were obtained at 77 K after outgassing for 10 h at 150 ºC under vacuum (10^{-5} torr) using a Micromeritics ASAP 2020. The specific surface area was obtained using the Brunauer-Emmett-Teller (BET) equation, taking 0.162 nm^2 as the cross-sectional area of the N_2 molecule.

The samples were studied by scanning electron microscopy (SEM) using a JSM5910-LV JEOL microscope. The mass ratio of the catalyst to the support and the atomic ratio between Ir and Ru in the electrocatalysts were analyzed by energy dispersive X-ray (EDX) microanalysis, using an INCA-300 energy analyzer coupled to the microscope.

Transmission electron microscopy (TEM) using a JEOL JEM-1400PLUS microscope operating at 120 kV and equipped with a GATAN US1000 CCD camera (2k x 2k) was applied for identification of the nanotube morphology and catalyst dispersion. The samples were also analyzed using a JEOL JEM-2100 LaB6 high-resolution TEM (HRTEM), operating at an accelerating voltage of 200 kV. Images were acquired and processed using the Digital Micrograph software by Gatan Inc., which allowed obtaining the FFT pictures and determining the interplanar spacings, which were contrasted with those listed in the data base [32]. The samples were dispersed in ethanol and ultrasonicated before deposition onto carbon coated copper grids for TEM analyses.

X-ray diffraction (XRD) was employed to characterize the crystal structure and the average crystallite size of the catalysts. The XRD diffractograms were obtained by a Bruker D8 Advance diffractometer operating with Cu K_α radiation (λ=1.5406 Å) and a 2θ scan from 5° to 80° (at 0.01° min^{-1}). The diffraction peaks were assigned according to the International Centre for Diffraction Data (ICDD) cards in PDF-2 database. The XRD data were used to determine the lattice parameters (from the interplanar distances, according to Bragg's law) and the average crystallite size by using Scherrer's equation.

X-ray photoelectron spectroscopy (XPS) analyses were performed using a Physical Electronics PHI 5500 Multitechnique System spectrometer with a monochromatic X-ray source (Al K_α line of 1486.6 eV, powered at 350 W). The samples were placed perpendicular to the analyzer axis. The external calibration was performed vs. the $3d_{5/2}$ line of Ag with a full width at half maximum (FWHM) of 0.8 eV, whereas the 1*s* line of the adventitious C was used for the internal calibration. The section for the surface analyses was a circular area of about 0.8 mm in diameter. The survey spectrum was obtained at 187.85 eV of Pass Energy and 0.8 eV/step and the high-resolution spectra at 23.5 eV of Pass Energy and 0.1 eV/step. A low energy electron gun less than 10 eV was used to neutralize for charging. The measurements were made in ultra high vacuum (UHV) chamber with pressure in the range 5.0×10^{-9}–2.0×10^{-8} torr. The corresponding spectra were analyzed using Ulvac-phi MultiPak V8.2B software. After a Shirley background correction, asymmetric and Gaussian-Lorentzian functions were used for fitting, constraining the FWHM of all the peaks and setting free the peak positions and areas.

2.3 Electrochemical characterization

The electrochemical measurements were conducted with a potentiostat PARSTAT 2273 (Ametek, Inc.) in a three-electrode glass cell with a gold working electrode 3 mm in diameter. Before each analysis, the tip of the gold disk electrode was polished to a mirror finish using alumina powder suspensions (0.3 μm and 0.05 μm, Buehler), followed by sonication in ultrapure water. An amount of 10 mg of the supported catalyst was dispersed in 0.5 mL mixture of isopropanol and ultrapure water (1:1) and sonicated for 30 min. A suitable amount of this dispersion was placed by means of micropipette onto the electrode to obtain a loading of about 35 μg cm^{-2} in IrO_2 or $IrRuO_x$. After drying under N_2 flow (Air Liquide, purity

99.995%), 5 μL of a 0.05 % solution of Nafion® in ethanol was placed on the top and dried also under N_2 flow. The reference electrode was $Hg/Hg_2SO_4/K_2SO_4$(sat) (Radiometer Analytical). However, all the potentials reported in this work are given with respect to the reversible hydrogen electrode (RHE). A Pt wire was used as the auxiliary electrode. The electrolyte was an aqueous solution of 0.50 mol dm^{-3} H_2SO_4 (prepared from Merck Suprapure), deaerated by N_2 bubbling for 20 min. The working temperature was 25.0 ± 0.1 ºC.

Cyclic voltammetry (CV) experiments were performed in the potential range of 0.100–1.400 V at a scan rate of 100 mV s^{-1} until a reproducible cyclic voltammogram was obtained. For the purposes of calculating the redox charge, consecutive cyclic voltammograms in the same potential range at scan rates of 200, 100, 50 and 20 mV s^{-1} were obtained. Our protocol was 20 cycles at 200 and 100 mV s^{-1}, 10 cycles at 50 mV s^{-1} and 5 cycles at 20 mV s^{-1}. The oxygen evolution was studied by linear sweep voltammetry (LSV), recording the anodic sweep between 1.200 and 2.000 V at scan rate of 1 mV s^{-1}. The *IR*-drop in the electrolyte was measured using electrochemical impedance spectroscopy at open circuit potential, from 100 kHz to 0.1 Hz with *ac* amplitude of 5 mV. All the voltammograms were corrected for the uncompensated resistance.

3. Results and discussion

3.1 Physico-chemical characterization of the materials

The specific surface area of TNTs and Nb-TNTs, determined from the BET adsorption/desorption isotherm, was found to be 145 and 260 m^2 g^{-1}, respectively, thus denoting the positive effect of Nb in increasing such a surface area. Note that these values are near to those of carbon Vulcan-XC72 (of about 250 m^2 g^{-1}) and significantly higher than those previously reported for $Nb_{0.05}Ti_{0.95}O_2$ powders (82.6 m^2 g^{-1}) [25] and mesoporous $Nb_{0.2}Ti_{0.8}O_2$ (132.4 m^2 g^{-1}) [22]. The effect of increasing the BET surface area was also described for Nb-doping of mesoporous titania [22], with values of 68 and 143 $m^2\ g^{-1}$ for 0.0 and 5.0 at% Nb, respectively, without significant changes for higher Nb contents. Adopting the same explanation, the increase in the BET surface area can be due to the different size of the titanium nano-building blocks obtained during the synthesis in aqueous media in the presence and in the absence of Nb, which become packed in a different form and led to different porous framework when submitted to calcination.

Tetragonal space group of rutile-type crystal lattice of IrO_2 (Fig. 1a) and $IrRuO_x$ (Fig. 1b) can be identified in the XRD patterns on both, the unsupported catalysts and the catalysts supported on the TNTs and the Nb-TNTs. Apart from these peaks the presence of the anatase phase of TNTs is also apparent, which is the titania structure produced during the synthesis procedure. The tendency for Nb-doped TiO_2 to form anatase has been previously reported in the literature [33], but the anatase phase was also formed in the absence of Nb-doping of the TNTs (Figs. 1a and b). Peaks located at 10.5º, 18º, 29º and 32º correspond to the lattice planes (200), (400), (600) and (001) of monoclinic titanates $H_2Ti_3O_7$ (the original phase of the support before calcination) [34]. The characteristic peak at around 2θ = 10º indicates the presence of a layered titanate and the small peak at 15º corresponds to small traces of sodium hexatitanate [35].

The XRD parameters corresponding to the specimens studied were calculated from the main peaks corresponding tho the lattice planes (110) and (101) by Bragg’s law and listed in Table 1. It is shown that both, the addition of Ru and the use of the TNTs produce a slight modification of the diffraction angles and thus, of the lattice parameters. The IrO_2 peaks were slightly shifted toward higher angles when introducing Ru and accordingly, the lattice parameters of $IrRuO_x$ are slightly smaller in comparison to IrO_2. This points out to the formation of a solid solution with a small lattice contraction [36,37], which is not surprising because the ionic radii of Ir^{4+} and Ru^{4+} are 0.0625 and 0.062 nm [37,38], respectively, the former being only slighlty greater. The use of the TNTs as supports also led to a slight decrease in the lattice parameters, thus indicating their binding effect on the IrO_2 and $IrRuO_x$ crystallites.

The average crystallite sizes of the catalysts, determined from the Scherrer equation [39] applied to the main two peaks (110) and (101), are also given in Table 1. It is shown that these values were also affected by the use of the TNTs as supports and the addition of Ru. The higher crystallite size of $IrRuO_x$ in comparison to IrO_2 can be attributed to the lower reactivity of the iridium chloride precursors with respect to those of ruthenium chloride. It has been described in the literature that the crystallite size of IrO_2 prepared by pyrolytic oxidation at 300–600 ºC of precursor deposits was significantly lower than that of RuO_2 prepared in the same form [40]. This was explained by the formation of stable iridium oxychlorides due to the partial oxidation of the most external part of the precursor, which limited the crystallite growth. On the contrary, in the case of RuO_2, this effect was minimized due to the higher reactivity of the Ru(III) chlorides and its oxidation intermediates. On the other hand, the crystallite size of the supported IrO_2 and $IrRuO_x$ catalysts was higher than that the unsupported samples. This can be explained by a structural effect of the support leading to the formation of a smaller number of larger crystallites, in contrast to the bigger number of smaller crystallites of the unsupported catalyst. A similar feature was previously described in the literature [21,39], which is probably related to the faster nucleation on the active sites of the given supports, due to a smaller energy barrier for the IrO_2 and $IrRuO_x$ nucleation, when compared to the homogeneous phase, thus favouring the crystallite growth. A further slight increase in the crystallite size of the catalysts for the Nb-doped TNTs in comparison to the non-doped TNTs is also observed, which could be related to the smaller values of the lattice parameters for the Nb-doped TNTs.

Fig. 2(a-d) shows TEM and HRTEM micrographs of the IrO_2/Nb-TNTs catalysts, respectively, in which the IrO_2 agglomerates and the Nb-doped nanotubes can be observed. Fig. 2(a and b) shows good dispersion of the catalyst agglomerates onto the nanotubes. Note that the latter are only easily identified in the pheripheral zones of the picture. Fig. 2(c) shows a magnification of a zone in which a nanotubular structure covered by IrO_2 is apparent. According to previous results in the literature, the continuity in the contact between the conductive IrO_2 particles is necessary for a good electronic conductivity of the supported catalyst, since titania is non-conductive [21,22,25]. Fig. 2(d) shows the HRTEM image of the catalyst, with the FFT picture of the squared marked area given in the inset. The points (1) and (2) gave d-spacing values of 0.40 nm, (3) and (4) of 0.49 nm and (5) and (6), of 0.33 nm. The latter matches well with the d-spacing in IrO_2, which is of 0.32 [32]. The former may be assigned to the titania support. These results are then in agreement with the XRD data reported above.

Fig. 2(e and f) is high resolution images of $IrRuO_x$/Nb-TNT, the first one showing the nanotubular form of the supports, which appeared to be covered by the deposited catalyst. Fig. 2(f) depicts its high resolution image, with the FFT picture obtained from the marked squared area given in the inset. The points (1) and (2) gave d-spacing values of 0.31 nm, (3) and (4) of 0.36 nm and (5) and (6) of 0.40 nm. Interplanar distance values of 0.32 nm for IrO_2 and RuO_2 rutile-type crystal lattices have been reported [32] and therefore, the first value matches well with the expected value for the d-spacing of $IrRuO_x$. The points (3)-(4) are close to the d-spacing value of 0.35 nm which have been reported for TiO_2 (anatase). The points (5) and (6) may also be assigned to the titania structures. These results are also in agreement with the XRD data reported above. The atomic ratios Ir:Ru of the supported and unsupported $IrRuO_x$ catalysts were determined by EDX and the corresponding results are listed in Table 2. It can be seen that the targeted Ir:Ru ratio of 60:40 is approached, in agreement with the stoichiometric values employed in the synthesis procedure.

The main XPS results are synthesized in Fig. 3, where the high-resolution spectra of the Ru 3*d* (a), Ti 2*p* (b), Nb 3*d* (c) and Ir 4*f* (d and e) photoelectron doublets are depicted and deconvoluted. It is worth to mention that Ir and Ru were detected in all the surface analyses performed at different points, thus indicating the good dispersion of the catalysts onto the supports, in agreement with the TEM observations. Fig. 3(a) shows the binding energy (BE) of surface carbon, which appears in the BE region of Ru and considered in the overall peak deconvolution. The Ru 3d region, with doublets at 281.7 and 286.1 eV, and at 283.1 and 288.0 eV, is compatible with anhydrous and hydrated RuO_2, respectively [41]. The Ti 2*p* peaks of IrO_2/TNT at 458.8 and 464.2 eV correspond to Ti(IV) [22,42] and it is shown a slight shift of these peaks to lower BEs when the support changes to Nb-TNTs (Fig. 3b). We tried to deconvolute these latter peaks into Ti(IV) and Ti(III) contributions, considering a BE doublet at 457.8 and 463.2 eV for the latter [22], but this was not feasible. Fig. 3(c) depicts the Nb 3*d* doublet, located at BE values of 206.7 and 209.3 eV, which can be related to Nb(IV) [42]. We tried also to deconvolute these peaks considering a possible contribution of Nb(V), with the lowest BE peak at 207.5 eV, because this was the oxidation state of Nb used in the synthesis procedure. However, it was neither feasible. In any case, the presence of this lower valence state of Nb in the oxide generates an electron donor level in the forbidden region of the bandgap of TiO_2, which would become a free electron in the conduction band of titania. The presence of these free electrons in the conduction band of the latter are important because they increase its conductivity [43] and then, Nb is in a suitable form.

Interesting results can also be observed in the Ir 4*f* photoelectron doublets of $IrRuO_x$ and IrO_2 blacks (Fig. 3d and e), which clearly show the coexistence of diferent oxidation states of Ir. As shown in Fig. 3(d), the deconvolution showed two doublets, the first at 62.5 and 65.5

eV, and the second at 63.8 and 67.1 eV, which could be assigned, respectively, to Ir(IV) and Ir(>IV) species [44,45], the latter being of the type $IrO_x(OH)_y$ [45]. The peak at BE of 68.8 eV can be considered a satellite peak [46]. It can also be shown in Fig. 3(d) that there was no shift of the binding energy of Ir in the presence of Ru. However, the relative amount of Ir(>IV) with respect to Ir(IV) was greater for unsupported $IrRuO_x$ than for unsupported IrO_2, 35 and 25 at% Ir(>IV), respectively. The relative amounts of Ir(>IV) with respect to Ir(IV) for IrO_2/TNT and IrO_2/Nb-TNT were 31 and 36 at%, which were also greater than for unsupported IrO_2. In addition, Fig. 3(e) shows that there is a slight shift of the Ir peak at 62.4 eV of IrO_2 black towards lower binding energies when supported on TNTs and 3Nb-TNTs and that this shift is more apparent for the latter. According to the literature [44], the BEs of the Ir(III) species of an IrO_x black catalysts prepared by an hydrothermal method were located at 61.8 and 64.7 eV. The valence states III, IV and VI of Ir were also reported for IrO_2 supported on mesoporous Nb-doped TiO_2 with high Nb contents, obtained by the Adams fusion method [22]. For this reason, the deconvolution was attempted including the Ir(III) doublet. However, the deconvolution was not then successful, thus suggesting that, if present, Ir(III) species should be in a very small amount.

3.2 Electrochemical characterization: accessibility and stability of the catalysts

Cyclic voltammograms of IrO_2 were obtained in deaerated H_2SO_4 0.50 mol dm^{-3} to evaluate their electrochemical surface properties and are depicted in Fig. 4(a). The anodic sweep was limited to 1.4 V to avoid O_2 evolution. The potential region between 0.1 and 0.4 V corresponds to the hydrogen adsorption (cathodic sweep) and desorption (anodic sweep), whereas for potentials above 0.4 V there is the adsorption/desorption of OH groups and Ir redox transitions [22,25,47]. There is a reversible peak at about 0.85 V corresponding to the Ir(III)/Ir(IV) redox couple, which is more apparent for the supported catalyst. It is interesting to observe that the peak current increases in the direction IrO_2 black < IrO_2/TNT < IrO_2/Nb-

TNT, thus indicating an increase in the number of active centers for oxygen evolution in the same direction, because the IrO_2 load deposited on these working electrodes was the same [22,48,49]. On the other hand, the Ir(IV)/Ir(>IV) redox transitions are expected to be about 1.2 V [22,47,48]. The same features can be observed in the cyclic voltammograms of Fig. 4(b) for the unsupported and supported $IrRuO_x$. There are obviously additional redox transitions corresponding to the Ru(III)/Ru(IV) and Ru(IV)/Ru(VI) couples at potentials about 0.6 and 0.8 V, the latter overlapping with the Ir peaks [50]. It is known that these redox transitions are responsible for the catalytic performance of IrO_2 and $IrRuO_x$ because the OER on these catalysts mainly proceeds along the electrochemical oxide path [22] and therefore, the charges related to these redox transitions are proportional to the active sites for the OER.

The curves shown in Fig. 4 correspond to pseudocapacitive behavior with high charge storage capacities. The areas under the anodic and over the cathodic current peaks of these voltammograms were determined at different scan rates to correlate the respective anodic and cathodic charges to the quantity of active sites or specific surface area of the different catalysts. The overall voltammetric charge can be divided into a fast and a slow charge. The former is due to the charging of the outer surface area of the electrode (q_{outer}), which shows the most accessible active sites on the catalyst surface at high scan rates. The slow charge is the total charge (q_{total}) and represents the total active sites because the non-accessible surface regions at high scan rates are accessible at low scan rates. In this form it is possible to find the outer and the total charge of the electrode [49,50]. The proton exchange between surface OH groups and the acidic electrolyte is considered to be rapid at “easily accessible” regions, whereas this exchange has some diffusion limitations within the inner regions. The outer charge can be determined by plotting the integrated total charge q vs. the inverse of the square root of the scan rate $v^{-1/2}$ (Eq. 1) and extrapolating the straigth line to zero ($v \rightarrow \infty$) [49,50]:

$$q = q_{\mathrm{outer}} + k' (v^{-1/2}) \quad (1)$$

In a similar way, Eq. 2 provides the total charge and the inner charge can then be easily calculated through Eq. 3.

$$q^{-1} = q^{-1}_{\text{total}} + k'' \, (v^{1/2}) \qquad (2)$$

$$q_{\text{total}} = q_{\text{outer}} + q_{\text{inner}} \qquad (3)$$

The corresponding results are reported in Table 3, where it is shown that the total charges of the supported materials are significantly higher than those of the unsupported ones. Note, however, that the crystallites of the former are larger than those of the latter (see Table 1), which would in principle suggest a smaller electrochemical surface area for the supported catalyst. However, this can be explained by the agglomeration of the smaller crystallites of the unsupported catalysts, thus decreasing the accessibility of the reactants to the catalyst surface. The bigger crystallites of the supported catalysts are better dispersed and the surface area of the catalyst is more accessible.

The anodic and cathodic redox transitions of Ir(III)/Ir(IV), Ir(IV)/Ir(>IV), Ru(III)/Ru(IV) and Ru(IV)/Ru(VI) of Fig. 4 take place at the same potential and the corresponding currents have a horizontal symmetry and therefore, they appear to be reversible. This reversibility can be further confirmed by determining the anodic-to-cathodic charge ratio q_A/q_C of the corresponding cyclic voltammograms, the system behaving reversibly when such a ratio approaches the unity, as previously found for IrO_2 [21,51]. This is the case for the q_A/q_C ratios of the unsupported and supported IrO_2 and $IrRuO_x$ catalysts listed in Table 3, which are very close to the unity regardless of the support and scan rates.

According to the above discussion, the values of $q_{\text{outer}}/q_{\text{total}}$ are a measurement of the catalyst accessibility and have been also summarized in Table 3. When IrO_2 is supported on TNTs and Nb-TNTs, the ratio $q_{\text{outer}}/q_{\text{total}}$ is slightly increased, thus indicating an increase in the amount of easier accessible active sites due to a better distribution onto the support surface. However, when IrRuOx is deposited onto Nb-TNTs, there is a decrease in the accessibility, but still keeping relatively high values of about 60%. On the contrary, $IrRuO_x$ deposited onto TNTs shows a rather low accessibility, which could be associated to a more compact catalyst layer, resulting in a bigger part of the catalyst active sites accessible only at lower scan rates. This is confirmed by the form of the cyclic voltammogram of $IrRuO_x$/TNT, which is relatively different in comparison to the voltammograms of the other catalysts (curve (2) in Fig. 4b).

In order to test and compare the stability, the catalysts were submitted to three consecutive linear sweep voltammograms starting at 1.2 V and ending at 2.0 V at 1 mV s^{-1}, the latter being sufficiently high to promote a huge O_2 evolution. The changes produced in the catalyst were evaluated by cyclic voltammetry in the same potential range as that used before the OER. The steady profiles were assured after five consecutive cyclic voltammograms at 20 mV s^{-1} and the last ones were used for the charge and accessibility calculations. These voltammograms are depicted in Fig. 5, the corresponding anodic and cathodic charges together with the accessibility are listed in Table 4, and the ratios between the charges after and before the OER are given in Table 5.

It is shown in Table 4 that the anodic to cathodic ratio q_A/q_C is all close to the unity except for supported $IrRuO_x$. When compared to the q_A/q_C data shown in Table 3 (before the OER), it appears that supported $IrRuO_x$ has lost a significant reversibility, in particular when supported on TNTs. On the other hand, the accessibility is maintained for unsupported IrO_2 and $IrRuO_x$ and also for IrO_2/Nb-TNT, with values of about 0.50, 0.75 and 0.65, respectively. For IrO_2/TNT, there is a loss of accessibility and therefore, it is less stable than IrO_2/Nb-TNT. For supported $IrRuO_x$, in spite that there is an increase in accessibility, the q_A/q_C decrease clearly indicates a stability loss after the OER.

As can be seen in Table 5, the outer, inner and total charges show a slight decrease after the OER, affecting in the same form the outer and inner charges, in unsupported IrO_2,

IrO_2/Nb-TNT and $IrRuO_x$, retaining 85%–95% of the total charge. For IrO_2/TNT the ratio of $q_{\text{inner after}}/q_{\text{inner before}}$ is clearly greater than the unity (1.35) and this corresponds to a decrease in the outer active surface area ($q_{\text{outer after}}/q_{\text{outer before}}$ of 0.36), thus meaning that part of the outer surface area becomes less accessible. Although when IrO_2 is supported onto TNTs the total surface area (charge) is increased (from about 520 to about 790 mC, see Tables 3 and 4), this support has not a stabilizing effect, the total anodic charge decreasing to 66% (Table 5). Destabilization due to the OER is also evidenced for supported $IrRuO_x$, in particular for $IrRuO_x$/TNT, where only 30% of the total charge is retained. For $IrRuO_x$/Nb-TNT the destabilization is lower and 63% of the total catalyst active sites were still active after the OER. Similar stabilizing effect of Nb addition to titania and Ru-based oxide electrodes has also been reported before in the literature [22,25,27,52–54]. Better stability is found for IrO_2/Nb-TNT, which keeps about 87% of the total charge, with some loss in the outer and in the inner charge values that are significantly higher than those for unsupported IrO_2 and therefore, the Nb-TNTs support has a stabilizing effect on IrO_2.

According to the data listed in Tables 3–5, the most stable catalysts are then, in decreasing order, unsupported $IrRuO_x$ > IrO_2/3Nb-TNT > unsupported IrO_2. However, IrO_2/Nb-TNT has to be preferred because of its highest outer and total anodic and cathodic charges both, before and after the consecutive linear sweep voltammograms.

3.3 Mechanism and performance

The first recorded linear sweep voltammograms of the IrO_2 and $IrRuO_x$ catalysts, corrected by the *IR*-drop, are shown in Figs. 6 and 7, respectively. Figs. 6(a) and 7(a) have been depicted by normalizing with respect to the electrode section. Figs. 6(b) and 7(b) have been normalized with respect to the total charge (see Table 3), which corresponds to the total number of active sites, because the total charge refers to the total amount of active sites that are accessible for oxygen evolution. The Tafel plots corresponding to these voltammograms are shown in the insets of Figs. 6 and 7, with the respective Tafel slopes listed in Table 6.

Two Tafel slopes have been identified for the OER, at low (about 1.0 mA cm^{-2}) and high current densities (over 10 mA cm^{-2}) and the corresponding values are given in Table 6. According to Table 6, at low current densities (below 1.0 mA cm^{-2}) the Tafel slopes for the IrO_2 samples are in the range from 0.049 to 0.054 V dec^{-1} whereas for the $IrRuO_x$ samples, in the range from 0.050 to 0.065 V dec^{-1}. At high current densities (over 10 mA cm^{-2}), the Tafel slopes for the IrO_2 samples range from 0.108 to 0.144 V dec^{-1}, whereas for the $IrRuO_x$ samples, from 0.122 to 0.150 V dec^{-1} (note that the same values can be obtained from Tafel plots of the insets in Figs. 6b and 7b). These values are similar to those already reported in the literature of 0.060 and 0.120 V dec^{-1} in the low and high overpotential current densities range, respectively [48,55,56]. Four possibilities were presented to explain the change in the anodic Tafel slope: 1) two different reaction pathways; 2) change in the electrode substrate; 3) change in the rate-determining step (rds); and 4) influence of potential controlled conditions.

In the acidic solution, the following reactions were generally proposed as the mechanism for oxygen evolution on active oxide electrodes [10,55,57,58]:

$$S + H_2O \rightarrow S\text{-}OH + H^+ + e^- \qquad (4)$$

$$S\text{-}OH \rightarrow S\text{-}O + H^+ + e^- \qquad (5)$$

$$S\text{-}OH + S\text{-}OH \rightarrow S\text{-}O + S + H_2O \qquad (6)$$

$$S\text{-}O + S\text{-}O \rightarrow O_2 + 2S \qquad (7)$$

where S stands for active sites on the oxide surface (Ir and Ru). It is known that the rds can be related to the values of the Tafel slopes. When the rds is the first electron transfer step (4), the Tafel slope is 120 mV dec^{-1}. When it is reaction (5) (dissociation of the O–H bond in the S–OH group), the Tafel slope is 40 mV dec^{-1}. In the case of reaction (6) (recombination of S-

OH) and (7) (recombination of S-O) being the rds, the respective Tafel slopes are of 30 and 15 mV dec^{-1}.

However, Tafel slopes in the range 60–120 mV dec^{-1} were reported in several papers in the literature [10,48,55,57–59]. To explain these values, a change was introduced in the mechanism, consisting in decomposing step (4) into the following two steps [55,57]:

$$S + H_2O \rightarrow S\text{-}OH^* + H^+ + e^- \qquad (8)$$

$$S\text{–}OH^* \rightarrow S\text{–}OH \qquad (9)$$

in which the intermediate S–OH is first formed as an unstable species (S–OH*). When step (8) is the rds, the Tafel slope is also 120 mV dec^{-1}, but when it is step (9), the Tafel slope becomes about 60 mV dec^{-1}. The mixed kinetic control of these two steps gives Tafel slopes in the range 60–120 mV dec^{-1}. This allowed interpreting the OER on Ti/IrO_2-Ta_2O_5 in H_2SO_4 [57], in which Tafel slopes of 59 and 130 mV dec^{-1} were reported for low and high current densities. The experimental curves fitted well in the low *j* range with a Tafel slope of 60 mV dec^{-1} when steps (8) and (9) were slow with respect to steps (5) –(7). On the other hand, a good fit was obtained in the high *j* region with a Tafel slope of 125 mV dec^{-1} when step (8) was the rds. Steps (5) and (6) occur in parallel and it is expected that, at low current densities, the amount of surface S-OH groups is small and therefore, step (5) is favoured. On the contrary, at high current densities the amount of surface S-OH groups is expected to be higher than at low current densities and then, step (6) should be favoured.

The results shown in Tables 6 and 7 strongly suggest that the OER at high current densities, for all the catalysts studied in this paper, is kinetically controlled through step (8). However, at low current densities and, as the Tafel slopes are in the range 40–60 mV dec^{-1}, the process appears to be limited by a mixed kinetic control through steps (9) and (5). In alkaline media, the Tafel slopes at current densities lower than 10 mA cm^{-2} were found to depend on the electrode material [2], being of 42 and 54.6 mV dec^{-1} for NiCu layered double hydroxide nanosheets on carbon cloth and on IrO_2/C, respectively. It is worth to note that these values are comparable to those obtained in the present work for acidic media, in which the mechanism can be somewhat different. It is also interesting to observe that the Tafel slopes in alkaline media depended on the electrode material and that the lower values strongly correlated with a higher catalytic activity [2]. This appears to be also the case for the catalysts studied in this work. According to the values given in Table 6, the smallest value of 49 mV dec^{-1} for IrO_2/3Nb-TNT suggests that step (5) plays a significant role as a limiting process, being faster as charge transfer is favored and we may therefore conclude that the charge transfer is facilitated in IrO_2/3Nb-TNT. A major feature contributing to this point appears then to be the increased conductivity of the support, due to the electron donor properties of Nb doping to the TNTs, which can accelerate the electron transfer, as also detected in alkaline electrolytes for different supports [2].

Table 6 also lists the potentials at which the current densities of 1 and 18 mA cm^{-2}, referred to the electrode section, are achieved. These values, as long as the catalyst loading was the same for all the samples tested, can be used to compare their catalyst activity. As shown in this table, when considering the IrO_2-based catalysts, IrO_2/Nb-TNT presents the smallest potential for both measured current densities and therefore, it should be the preferred one. Smaller potential values were obtained for the $IrRuO_x$-based catalyst at 1 mA cm^{-2} when compared to the IrO_2-based catalysts, but this is not the case for 18 mA cm^{-2}, where only $IrRuO_x$/Nb-TNT presents the smallest one. As discussed before, the mechanism presents some change at high current densities and this might justify some variation in the sequence of potentials. In the low current density region, when the specific current density is referred to the total charge, the same potential trend as in the case of 1 mA cm^{-2} is found. However, in the high current density region, when extrapolating from the Tafel plots, the exchange current densities are the highest for IrO_2/Nb-TNT, with 20.4 mA C^{-1}, followed by $IrRuO_x$/Nb-TNT with 16.5 mA C^{-1}. Therefore, it is appreciated that IrO_2/Nb-TNT has somewhat better catalyst activity than $IrRuO_x$/Nb-TNT (Table 6) and also it has a better stability (Table 5).

The performance of the catalysts studied in this work has been compared to that for different catalysts reported in the literature. Here should be noted that such a comparison is not easy due to the variety of catalyst loadings and experimental conditions such as the electrolyte and sweep rate. However, a comparison is attempted in terms of the potential at which the current densities are of 1 and 18 mA cm^{-2} (see Tables 6 and 7). Data shown in Table 7 have been obtained as reported values in previous papers or measured from their corresponding plots at 25 ºC. It is shown in Table 7 that for unsupported IrO_2 the potentials at 1 mA cm^{-2} are about 1.48 V, comparable but somewhat higher than that obtained in this work of 1.47 V, although the oxide loading is smaller by 7–30 times (Table 6). On the other hand, increasing the IrO_2 content of the supported catalyst up to 33 wt%, the potential at 1 mA cm^{-2} decreases to 1.43 V (Table 7), which is somewhat smaller than our result of 1.45 V (Table 6) for a 7-times smaller oxide loading, although with a higher content of 50 wt% of IrO_2 in the catalyst. Note also that the potential value of this work at 18 mA cm^{-2} for the Nb-doped support and 50 wt% IrO_2 (1.543 V, Table 6) is smaller than those for a higher percentage of Nb although with the smaller amount of 40 wt% IrO_2 (1.56 and 1.58 V, Table 7).

When considering the unsupported $IrRuO_x$ and other particles using different alloying elements such as Co, Sn and Ta, the situation continues to be favourable to the unsupported $IrRuO_x$ reported in Table 6, with values of 1.442 and 1.554 V at 1 and 18 mA cm^{-2}, respectively, which are smaller than those reported for the former in Table 7. The situation is repeated for supported $IrRuO_x$ on TNTs and Nb-TNTs, with smaller potential values at 1 mA cm^{-2} with respect to that supported on ATO.

The results of Table 7 have been also compared to those obtained previously in the literature for non-noble based catalysts in strongly alkaline solutions [1–5]. Overpotentials in the range 0.26–0.45 V, which correspond to potentials of 1.49–1.68 V, have been generally reported for current densities of 10 mA cm^{-2} in 0.1–1.0 M KOH [1–3]. The potential values fall within the range corresponding to 1–18 mA cm^{-2} listed in Tables 6 and 7. However, impressive current densities of 50 mA cm^{-2} have been reported for overpotentials of 0.276 V in 1.0 M KOH [5] and even 200 mA cm^{-2} at 1.47 V in 5.0 M KOH [4] for integrated NiFe-based catalysts grown on Ni foam, thus denoting the importance of the close contact between catalyst and support for an efficient charge transfer and having potential industrial applications.

Considering together all the results obtained in this work, which are those concerning the number of active sites, the catalyst dispersion, stability and the electrode potential corresponding to given current densities, the IrO_2/Nb-TNT catalyst is the most promising candidate for the OER in PEMWEs. According to the results of the present paper, the good performance of IrO_2/Nb-TNT can be assigned to the good dispersion of IrO_2 on the high-specific-surface-area Nb-doped supports, thus allowing a good accessibility of the active centers of the catalyst, to its increased stability with respect to the absence of Nb doping and to the electron donor properties of the Nb(IV) oxide species to the conduction band of titania. Further work using a greater amount of Nb doping and adjusting the wt% of IrO_2 on the support is planned to optimize the catalyst for the best performance together with the corresponding stability tests in real devices.

4. Conclusions

IrO_2 and $IrRuO_x$ (Ir:Ru 60:40 at%) catalysts were synthesized and supported by 50 wt% onto titania nanotubes and (3 at% Nb) Nb-doped titania nanotubes. The resulting materials, unsupported IrO_2 and $IrRuO_x$, IrO_2/TNT, IrO_2/Nb-TNT, $IrRuO_x$/TNT and $IrRuO_x$/Nb-TNT, were characterized by means of XRD, SEM(EDX), TEM, HRTEM, XPS and tested electrochemically toward oxygen evolution reaction in a three-electrode cell.

The BET surface areas of the TNTs and the Nb-TNTs were 145 and 260 m^2 g^{-1}, respectively, the latter being higher than that of Nb-doped titania supports previously reported in the literature. The use of TNTs and Nb-TNTs as supports led to a decrease in the lattice parameters of IrO_2 and $IrRuO_x$ crystallites. In addition, the crystallite size increased in the order: unsupported catalyst < TNTs-supported < Nb-TNTs-supported. These structural effects appear to be related to the binding effect of the supports and to the easier nucleation of the catalysts in the same order. The TEM and XPS results showed a good coverage of the titania nanotubes by the catalysts. The XPS analyses indicated that Nb was mainly present as Nb(IV) oxide species, thus behaving as a donor introducing free electrons to the conduction band of titania.

The redox transitions of the cyclic voltammograms were interpreted according to the XPS analyses and the measurement of the charges involved allowed concluding that they were reversible. Despite the supported materials presented bigger crystallite sizes than the unsupported ones, the total number of active sites of the former was also higher due to their better catalyst dispersion on the high surface area of the titania nanotubes and therefore, they presented a better performance toward the OER. Considering i) the outer and the total anodic and cathodic charges of the cyclic voltammograms in the range 0.1–1.4 V, ii) the stability of the catalysts before and after three consecutive linear sweep voltammograms from 1.2 to 2.0 V and iii) the electrode potentials at given current densities of 1 and 18 mA cm^{-2} and 1 mA C^{-1}, the preferred catalyst was IrO_2/Nb-TNT. The electrode potentials corresponding to these current densities were between the smallest ones given in the literature despite the small oxide loading used in this work and its Nb doping, thus making the IrO_2/Nb-TNT catalyst a promising candidate for the OER in PEMWEs. The good performance of IrO_2/Nb-TNT was assigned to different factors: good dispersion and accessibility of the IrO_2 nanoparticles, increased stability and high specific surface area of the Nb-doped support and the electron donor properties of the Nb(IV) oxide species to the conduction band of titania.

Acknowledgments

The authors would like to thank to EU FP7 SUSHGEN Network project No. 238678 and project ENE2017-83976-C2-1-R (AEI/FEDER, EU)). The facilities of the *Centres Científics i Tecnològics de la Universitat de Barcelona* (CCiT-UB) are also acknowledged for the structural and surface analyses.

References

[1] J. Qi, W. Zhang, R. Cao, Adv. Energy Mater. 8 (2018) 1701620.

[2] Y. Zheng, J. Qiao, J. Yuan, J. Shen, A. Wang, P.Gong, X. Weng, L. Niu, Electrochim. Acta 282 (2018) 735–742.

[3] L. Xu, Y. Zou, Z. Xiao, S. Wang, J. Energy Chem. 35 (2019) 24–29.

[4] W. Zhang, J. Qi, K. Liu, R. Cao, Adv. Energy Mater. 6 (2016) 1502489.

[5] D. Guo, J. Qi, W. Zhang, R. Cao, ChemSusChem 9 (2016) 1–8.

[6] J. Xu, Q. Li, M.K. Hansen, E. Christensen, A.L.T. García, G. Liu, X. Wang, N.J. Bjerrum, Int. J. Hydrogen Energy 37 (2012) 18629–18640.

[7] R.E. Fuentes, J. Farell, J.W. Weidner, Electrochem. Solid-State Lett. 14 (2011) E5–E7.

[8] Q. Xue, W. Gao, J. Zhu, R. Peng, Q. Xu, P. Chen, Y. Chen, J. Colloid Interf. Sci. 529 (2018) 325–331.

[9] M. Carmo, D.L. Fritz, J. Mergel, D. Stolten, Int. J. Hydrogen Energy 38 (2013) 4901–4934.

[10] E. Tsuji, A. Imanishi, K.-I. Fukui, Y. Nakato, Electrochim. Acta 56 (2011) 2009–2016.

[11] G. Wei, Y. Wang, C. Huang, Q. Gao, Z. Wang, L. Xu, Int. J. Hydrogen Energy 35 (2010) 3951–3958.

[12] D. Labou, E. Slavcheva, U. Schnakenberg, S. Neophytides, J. Power Sources 185 (2008) 1073–1078.

[13] S. Song, H. Zhang, X. Ma, Z. Shao, R.T. Baker, B. Yi, Int. J. Hydrogen Energy 33 (2008) 4955–4961.

[14] J.C. Cruz, V. Baglio, S. Siracusano, R. Ornelas, L. Ortiz-Frade, L.G. Arriaga, V. Antonucci, A.S. Aricò, J. Nanopart. Res. 13 (2011) 1639–1646.

[15] S. Siracusano, V. Baglio, A. Di Blasi, N. Briguglio, A. Stassi, R. Ornelas, E. Trifoni, V. Antonucci, A.S. Aricò, Int. J. Hydrogen Energy 35 (2010) 5558–5568.

[16] E. Rasten, G. Hagen, R. Tunold, Electrochim. Acta 48 (2003) 3945–3952.

[17] V. Baglio, A. Di Blasi, T. Denaro, V. Antonucci, A.S. Aricò, R. Ornelas, F. Matteucci, G. Alonso, L. Morales, G. Orozco, L.G. Arriaga, J. New Materials for Electrochem. Systems 11 (2008) 105–108.

[18] A. Di Blasi, C. D´Urso, V. Baglio, V. Antonucci, A.S. Aricò, R. Ornelas, F. Matteucci, G. Orozco, D. Beltran, Y. Meas, L.G. Arriaga, J. Appl. Electrochem. 39 (2009) 191–196.

[19] A.T. Marshall, S. Sunde, M. Tsypkin, R. Tunold, Int. J. Hydrogen Energy 32 (2007) 2320–2324.

[20] A. Marshall, B. Børrensen, G. Hagen, M. Tsypkin, R. Tunold, Electrochim. Acta 51 (2006) 3161–3167.

[21] P. Mazúr, J. Polonský, M. Paidar, K. Bouzek, Int. J. Hydrogen Energy 37 (2012) 12081–12088.

[22] C. Hao, H. Lv, C. Mi, Y. Song, J. Ma, ACS Sustainable Chem. Eng. 4 (2016) 746–756.

[23] Y.-C. Nah, I. Paramasivam, P. Schmuki, ChemPhysChem 11 (2010) 2698–2713.

[24] B.J. Morgan, D.O. Scanlon, G.W. Watson, J. Mater. Chem. 19 (2009) 5175–5178.

[25] W. Hu, S. Chen, Q. Xia, Int. J. Hydrogen Energy 39 (2014) 6967–6976.

[26] T. Kasuga, Thin Solid Films 496 (2006) 141–145.

[27] E. Sotter, X. Vilanova, E. Llobet, M. Stankova, X. Correig, J. Optoelectron. Adv. M. 7 (2005) 1395–1398.

[28] S.L. Gojković, B.M. Babić, V.R. Radmilović, N.V. Krstajić, J. Electroanal. Chem. 639 (2010) 161–166.

[29] L. Xiong, A. Manthiram, Electrochim. Acta 49 (2004) 4163–4170.

[30] A. Zlotorowicz, F. Seland, S. Sunde, ECS Trans. 50 (2013) 71–84.

[31] J.C. Cruz, A. Ramos Hernández, M. Guerra-Balcazar, A.U. Chávez-Ramirez, J. Ledesma-García, L.G. Arriaga, Int. J. Electrochem. Sci. 7 (2012) 7866–7876.

[32] http://database.iem.ac.ru/mincryst/. Accessed on 7th of February 2019.

[33] J. Arbiol, J. Cerdà, G. Dezanneau, A. Cirera, F. Peiró, A. Cornet, J.R. Morante, J. Appl. Phys. 92 (2002) 853.

[34] C.-K. Lee, S.-S. Liu, H.-C. Chen, Recent Pat. Nanotech. 3 (2009) 203–212.

[35] R.A. Zárate, S. Fuentes, A.L. Cabrera, V.M. Fuenzalida, J. Crystal Growth 310 (2008) 3630–3637.

[36] S. Siracusano, N. Van Dijk, E. Payne-Johnson, V. Baglio, A.S. Aricò, Appl. Catal., B 164 (2015) 488–495.

[37] J. Cheng, H. Zhang, G. Chen, Y. Zhang, Electrochim. Acta 54 (2009) 6250–6256.

[38] R.D. Shannon, Acta Crystallogr. Sect. A 32 (1976) 751–767.

[39] V.K. Puthiyapura, S. Pasupathi, H. Su, X. Liu, B. Pollet, K. Scott, Int. J. Hydrogen Energy 39 (2014) 1905–1913.

[40] A. De Battisti, G. Lodi, L. Nanni, G. Battaglin, A. Benedetti, Can. J. Chem. 75 (1997) 1759–1765.

[41] J.L. Gómez de la Fuente, F.J. Pérez-Alonso, M.V. Martínez-Huerta, M.A. Peña, J.L.G. Fierro, S. Rojas, Catal. Today 143 (2009) 69–75.

[42] M.V. Nogueira, G.M.M.M. Lustosa, Y. Kobayakawa, W. Kogler, M. Ruiz, E.S.M. Filho, M.A. Zaghete, L.A. Perazolli, Adv. Mater. Sci. Eng. 2018, 7326240.

[43] Y. Liu, J.M. Szeifert, J.M. Feckl, B. Mandlmeier, J. Rathousky, O. Hayden, D. Fattakhova-Rohlfing, T. Bein, ACS Nano 4 (2010) 5373–5381.

[44] G.C. da Silva, N. Perini, E.A. Ticianelli, Appl. Catal., B 218 (2017) 287–297.

[45] L. Preda, T. Kondo, T. Spataru, M. Marin, M. Radu, P. Osiceanu, A. Fujishima, N. Spataru, ChemElectroChem 4 (2017) 1908–1915.

[46] L. Atanasoska, R. Atanasoski, S. Trasatti, Vacuum 40 (1990) 91–94.

[47] E. Kuznetsova, V. Petrykin, S. Sunde, P. Krtil, Electrocatalysis 6 (2015) 198–210.

[48] S. Siracusano, V. Baglio, C. D'Urso, V. Antonucci, A.S. Aricò, Electrochim. Acta 54 (2009) 6292–6299.

[49] S. Ardizzone, G. Fregonara, S. Trasatti, Electrochim. Acta 35 (1990) 263–267.

[50] T. Audichon, E. Mayousse, S. Morisset, C. Morais, C. Comminges, T.W. Napporn, K.B. Kokoh, Int. J. Hydrogen Energy 39 (2014) 16785–16796.

[51] C.P. De Pauli, S. Trasatti, J. Electroanal. Chem. 396 (1995) 161–168.

[52] M.H.P. Santana, L.M. Da Silva, L.A. De Faria, Electrochim. Acta 48 (2003) 1885–1891.

[53] V.K. Puthiyapura, S. Pasupathi, S. Basu, X. Wu, H. Su, N. Varagunapandiyan, B. Pollet, K. Scott, Int. J. Hydrogen Energy 38 (2013) 8605–8616.

[54] M. Lira-Cantu, M.K. Siddiki, D. Muñoz-Rojas, R. Amade, N.I. González-Pech, Sol. Energy Mater Sol. Cells 94 (2010) 1227–1234.

[55] L.A. De Faria, J.F.C. Boodts, S. Trasatti, J. Appl. Electrochem. 26 (1996) 1195–1199.

[56] J.L. Corona-Guinto, L. Cardeño-García, D.C. Martínez-Casillas, J.M. Sandoval-Pineda, P. Tamayo-Meza, R. Silva-Casarin, R.G. González-Huerta, Int. J. Hydrogen Energy 38 (2013) 12667–12673.

[57] J.-M. Hu, J.-Q. Zhang, C.-N. Cao, Int. J. Hydrogen Energy 29 (2004) 791–797.

[58] T. Reier, D. Teschner, T. Lunkenbein, A. Bergmann, S. Selve, R. Kraehnert, R. Schlögl, P. Strasser, J. Electrochem. Soc. 161 (2014) F876–F882.

[59] L. Ouattara, S. Fierro, O. Frey, M. Koudelka, C. Comninellis, J. Appl. Electrochem. 39 (2009) 1361–1367.

[60] A. Marshall, B. Børresen, G. Hagen, M. Tsypkin, R. Tunold, Energy 32 (2007) 431–436.

[61] A.T. Marshall, R.G. Haverkamp, Electrochim. Acta 55 (2010) 1978–1984.

Table 1 Average crystallite size and lattice parameters of IrO_2, $IrRuO_x$ and TNTs-supported IrO_2 and $IrRuO_x$ cataysts.

Catalyst	**(110) peak** (degree)	**(101) peak** (degree)	**lattice parameter a=b** (nm)	**lattice parameter c** (nm)	**crystallite size** (nm)
IrO_2 black	27.91	34.79	4.517	3.152	7.38
IrO_2/TNT	28.03	34.87	4.496	3.131	9.78
IrO_2/Nb-TNT	28.03	34.94	4.493	3.118	10.67
$IrRuO_x$ black	28.01	35.00	4.501	3.119	8.96
$IrRuO_x$/TNT	28.09	35.06	4.489	3.115	14.00
$IrRuO_x$/Nb-TNT	28.05	35.07	4.492	3.105	14.37

Table 2 Ir:Ru atomic ratio measured by EDX.

Composition	Ir (at%)	Ru (at%)
$IrRuO_x$	58.7	41.3
$IrRuO_x$/TNT	57.8	42.2
$IrRuO_x$/Nb-TNT	56.6	43.4

Table 3 Outer (q_{outer}), inner (q_{inner}) and total anodic (q_A) and cathodic (q_C) charges of the IrO_2 and $IrRuO_x$ catalysts, measured from the cyclic voltammograms of Fig. 4 (before the OER stability test).

Catalyst	q_{outer} (mC)	q_{inner} (mC)	q_A (mC)	q_C (mC)	q_A/q_C	**accessibility** q_{outer}/q_{total}
IrO_2	272	265	537	503	1.07	0.50
IrO_2/TNT	543	239	782	794	0.98	0.69
IrO_2/Nb-TNT	602	360	962	962	1.00	0.63
$IrRuO_x$	270	88.3	358	347	1.03	0.75
$IrRuO_x$/TNT	149	713	862	847	1.02	0.17
$IrRuO_x$/Nb-TNT	279	176	455	442	1.03	0.61

Table 4 Outer, inner and total charges of IrO_2 and $IrRuO_x$ based catalysts after recording consecutive linear sweep voltammograms.

Catalyst	**outer charge (**q_{outer}**)** (mC)	**inner charge (**q_{inner}**)** (mC)	**total anodic charge (**q_A**)** (mC)	**total cathodic charge (**q_C**)** (mC)	q_A/q_C	**accessibility** q_{outer}/q_{total}
IrO_2	229	220	448	455	0.98	0.51
IrO_2/TNT	195	323	518	543	0.95	0.38
IrO_2/Nb-TNT	538	295	833	826	1.01	0.65
$IrRuO_x$	252	92.5	345	346	1.00	0.73
$IrRuO_x$/TNT	61.7	201	262	455	0.57	0.24
$IrRuO_x$/Nb-TNT	243	40.7	284	355	0.80	0.86

Table 5 Outer, inner and total charge ratios of the IrO_2 and $IrRuO_x$ based catalysts after and before the consecutive linear sweep voltammograms.

Catalyst	$q_{\text{outer after}}/q_{\text{outer before}}$	$q_{\text{inner after}}/q_{\text{inner before}}$	$q_{\text{A total after}}/q_{\text{A total before}}$
IrO_2	0.84	0.83	0.83
IrO_2/TNT	0.36	1.35	0.66
IrO_2/Nb-TNT	0.89	0.82	0.87
$IrRuO_x$	0.93	1.05	0.96
$IrRuO_x$/TNT	0.41	0.28	0.30
$IrRuO_x$/Nb-TNT	0.87	0.23	0.63

Table 6 Electrode potentials *E* and tafel slopes *b* calculated from the *E* – log *j* plots of the polarization curves shown in Figs. 6a and 7a, in the low and high *j* regions. The electrode potentials and the estimated specific exchange current densities j_0 corresponding to Figs. 6b and 7b are also indicated.

	Low *j*			**High *j***		
Catalyst	*E* at 1 mA cm^{-2} (V)	*b* (V dec^{-1})	*E* at 1 mA C^{-1} (V)	*E* at 18 mA cm^{-2} (V)	*b* (V dec^{-1})	j_0 (mA C^{-1})
IrO_2	1.467	0.054	1.35	1.584	0.144	6.6
IrO_2/TNT	1.455	0.052	1.36	1.553	0.108	8.3
IrO_2/Nb-TNT	1.449	0.049	1.36	1.543	0.114	20.4
$IrRuO_x$	1.442	0.050	1.33	1.554	0.136	3.8
$IrRuO_x$/TNT	1.452	0.065	1.31	1.586	0.150	10.4
$IrRuO_x$/Nb-TNT	1.408	0.054	1.29	1.526	0.122	16.5

Table 7. Potentials at current densities 1 and 18 mA cm^{-2} for different IrO_2 and RuO_2-based catalysts taken from the literature for the OER at 25 ºC in three-electrode cell (references in square brackets).

Catalyst	**Oxide loading** (mg cm^{-2})	**Electrolyte**	***v*** (mV s^{-1})	***E*** **(1 mA cm^{-2})** (V)	**E (18 mA cm^{-2})** (V)
IrO_2 particles [60]	1.00	0.5M H_2SO_4	SS[a]	1.475	-
Unsupported IrO_2 [25]	0.255	id	5	1.48	-
IrO_2(17 wt.%)/$Nb_{0.05}Ti_{0.95}O_2$ [25]	0.255	id	id	1.53	-
IrO_2(26 wt.%)/$Nb_{0.05}Ti_{0.95}O_2$ [25]	0.255	id	id	1.50	-
IrO(33 wt.%)/$Nb_{0.05}Ti_{0.95}O_2$ [25]	0.255	id	id	1.43	-
IrO_2(20 wt.%)/ATO[b] [61]	0.16	id	0.5	1.488	-
Ir/CNB[c] [8]	0.02[d]	0.1M $HClO_4$	5	-	1.55
IrO_2(40 wt.%)/$Nb_{0.2}Ti_{0.8}O_2$ [22]	0.092	id	5	-	1.56
IrO_2(40 wt.%)/$Nb_{0.05}Ti_{0.95}O_2$ [22]	0.092	id	id	-	1.58
$Ru_{0.9}Ir_{0.1}O_2$ particles [50]	0.38	0.5M H_2SO_4	id	1.445	-
$Ir_{0.6}Ru_{0.4}O_2$ particles [60]	1.00	id	SS[a]	1.463	-
RuIrOx powder [56]	0.064[d]	id	20	1.52	1.66
RuIrCoOx powder [56]	0.064[d]	id	20	1.53	1.64
$Ir_{0.7}Sn_{0.3}O_2$ particles [14]	0.78	id	SS[a]	1.500	-
$Ir_{0.7}Ta_{0.3}O_2$ particles [53]	0.70	id	SS[a]	1.488	-
RuO_2(20 wt.%)/ATO[b] [61]	0.16	id	0.5	1.427	-
$Ir_{0.5}Ru_{0.5}O_2$(20 wt.%)/ATO[b] [61]	0.16	id	0.5	1.461	-

[a] Steady State

[b] Sb-doped SnO_2

Figure captions

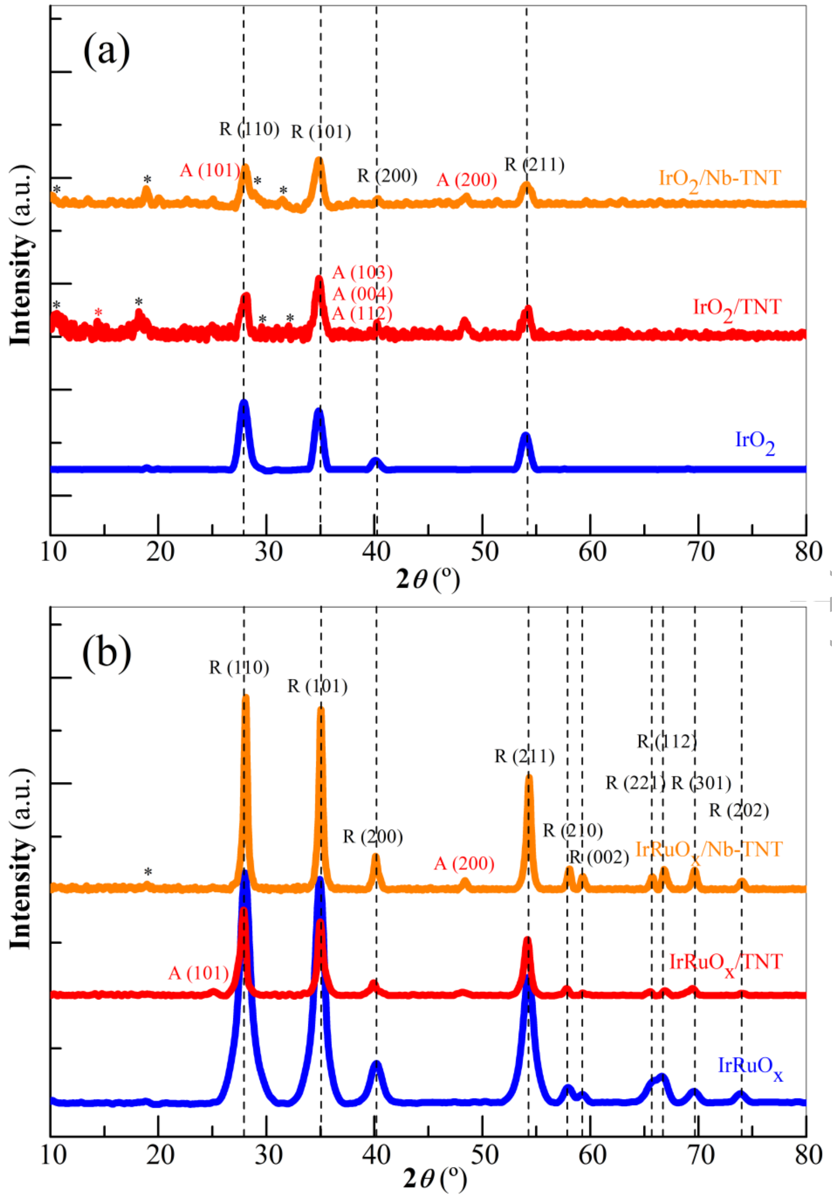

Fig. 1. X-ray diffractograms of (a) IrO_2 and (b) $IrRuO_x$, unsupported and supported onto TNTs and Nb-TNTs catalysts. Rutile phase of IrO_2 is denoted by R and anatase phase of TNTs, with A (marked with * the titanate peaks of the support).

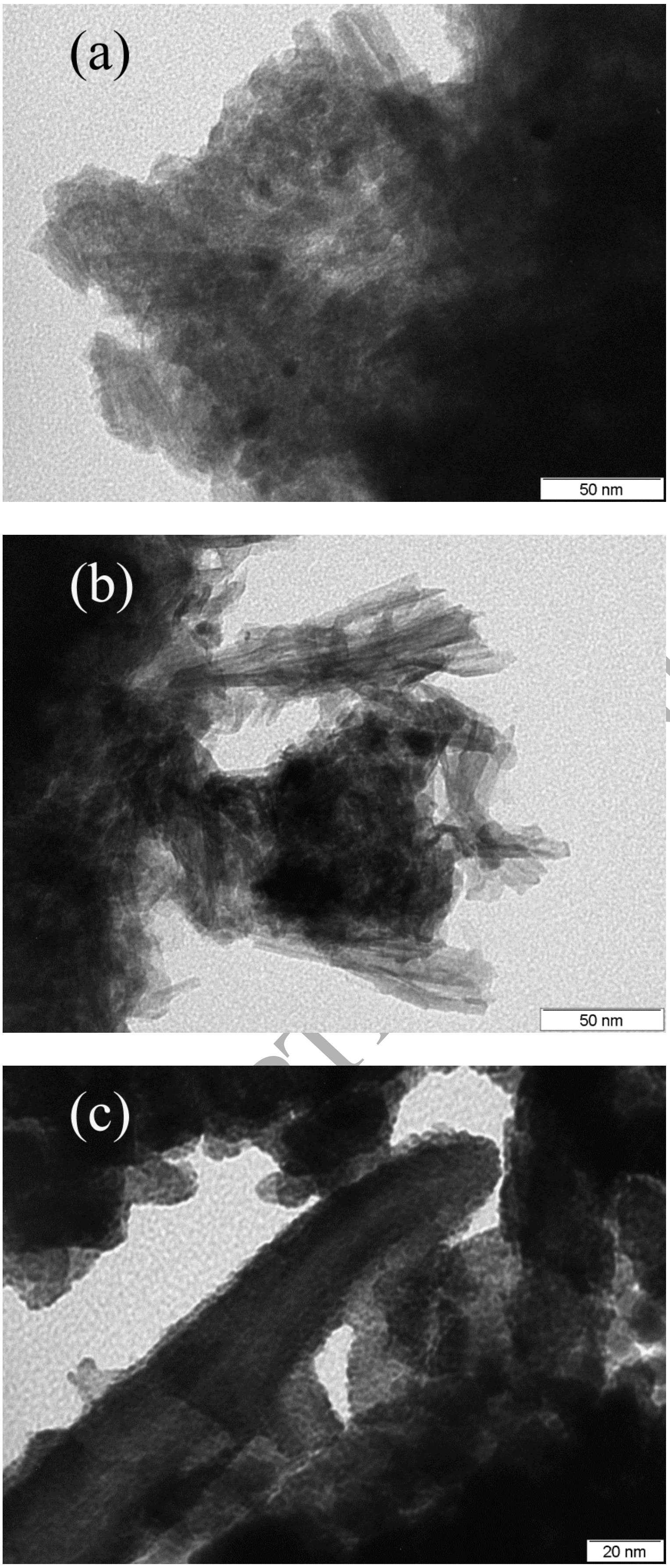
(a)
50 nm
(b)
50 nm
(c)
20 nm

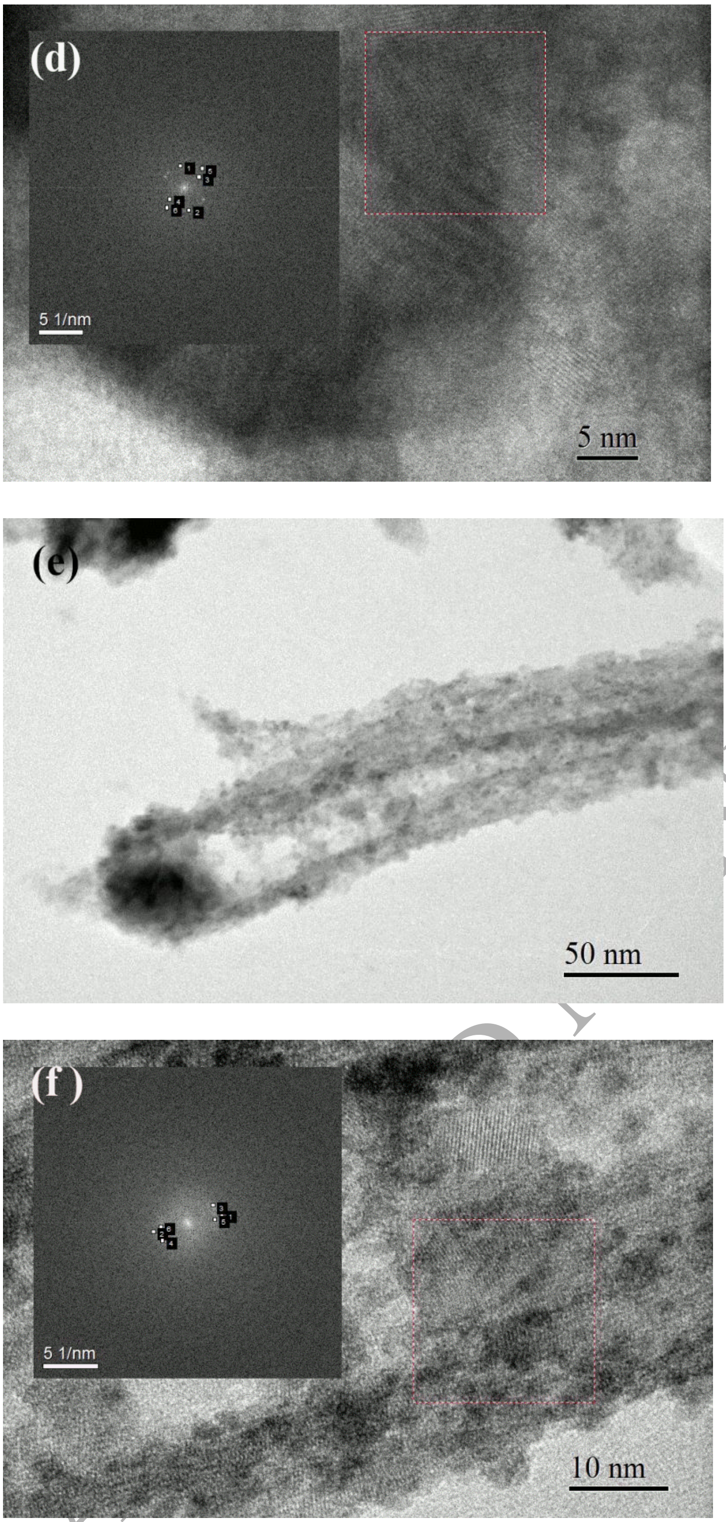

Fig. 2. Selected TEM images of (a)-(d) IrO_2/Nb-TNT and (e)-(f) $IrRuO_x$/Nb-TNTs at different sample regions. (a)-(c) are focused on the catalyst dispersion, the catalyst coverage onto Nb-TNTs and the nanotubular structures, respectively; (d) HRTEM image of IrO_2/Nb-TNT (the inset corresponding to the FFT picture of the depicted squared area). (e) Image of the

nanotubular structure of IrRuO$_x$/Nb-TNTs, where the nanotubes are covered by the catalyst and (f) HRTEM image of IrRuO$_x$/Nb-TNT (the inset corresponding to the FFT picture of the depicted squared area).

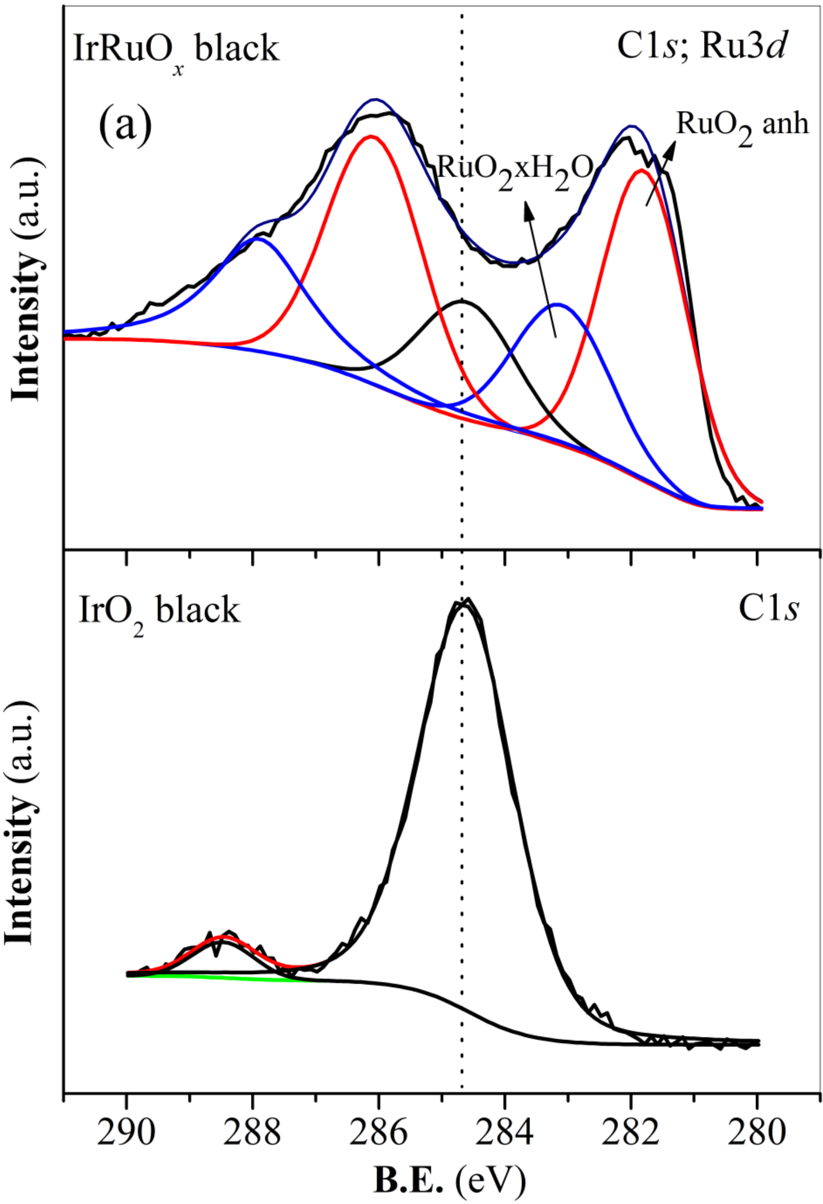

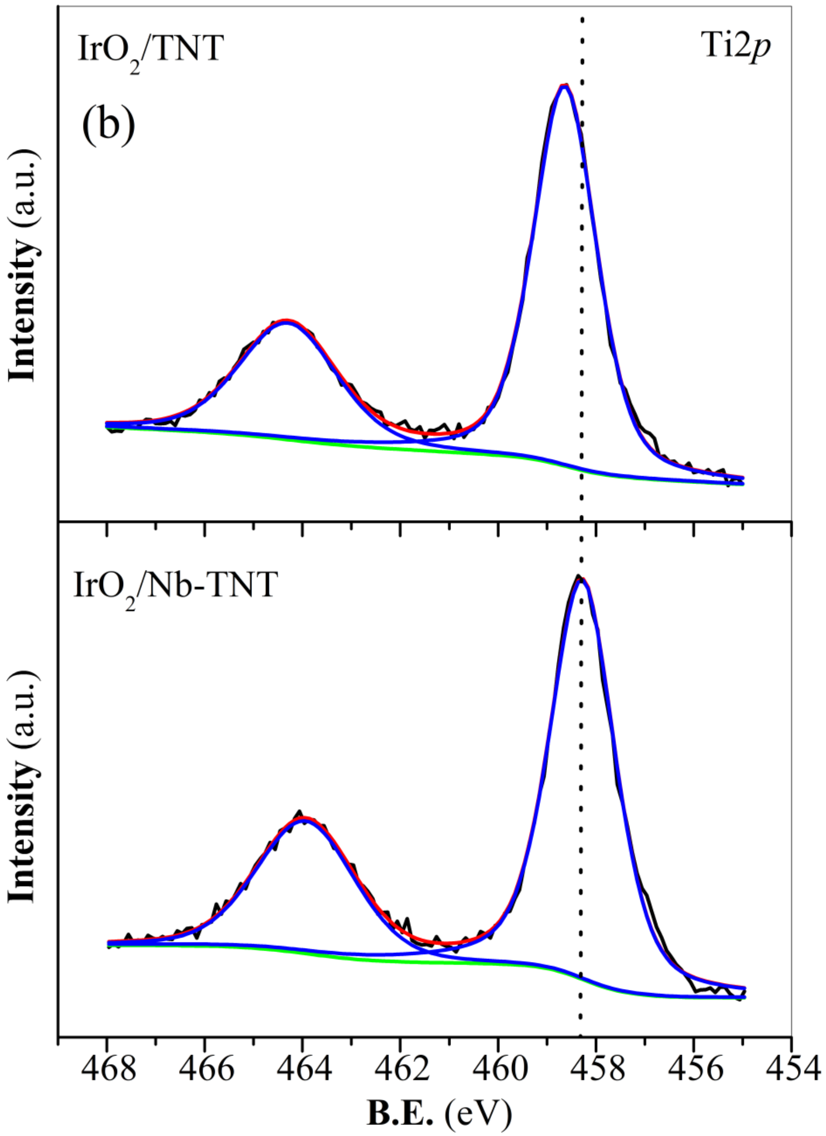
IrO₂/TNT
Ti2p
(b)
Intensity (a.u.)
IrO₂/Nb-TNT
Intensity (a.u.)
468
466
464
462
460
458
456
454
B.E. (eV)

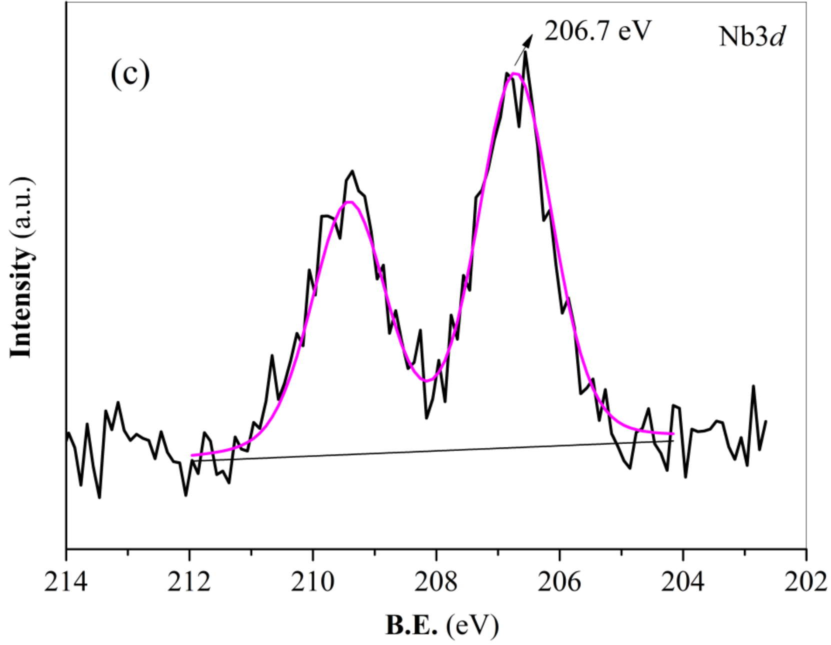
(c)
206.7 eV
Nb3d
Intensity (a.u.)
214
212
210
208
206
204
202
B.E. (eV)

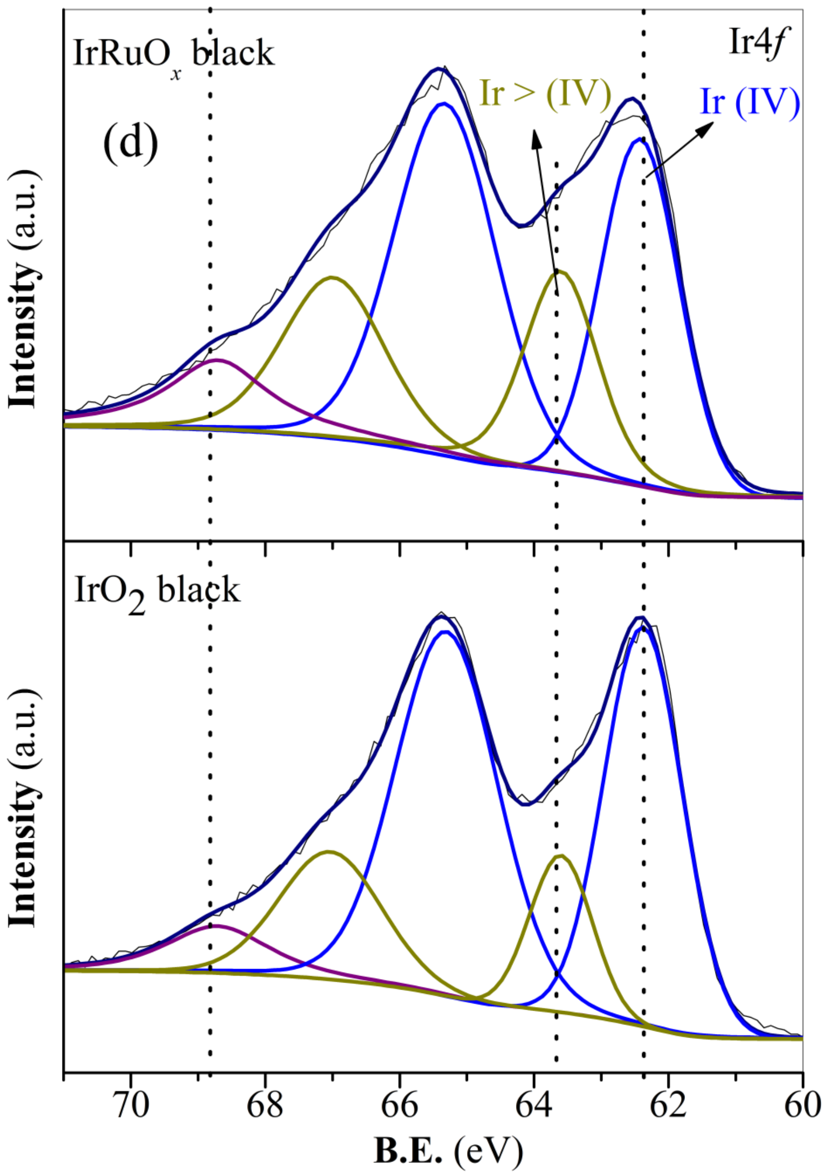
IrRuO$_x$ black
(d)
Ir4*f*
Ir > (IV)
Ir (IV)
IrO$_2$ black
Intensity (a.u.)
Intensity (a.u.)
70
68
66
64
62
60
B.E. (eV)

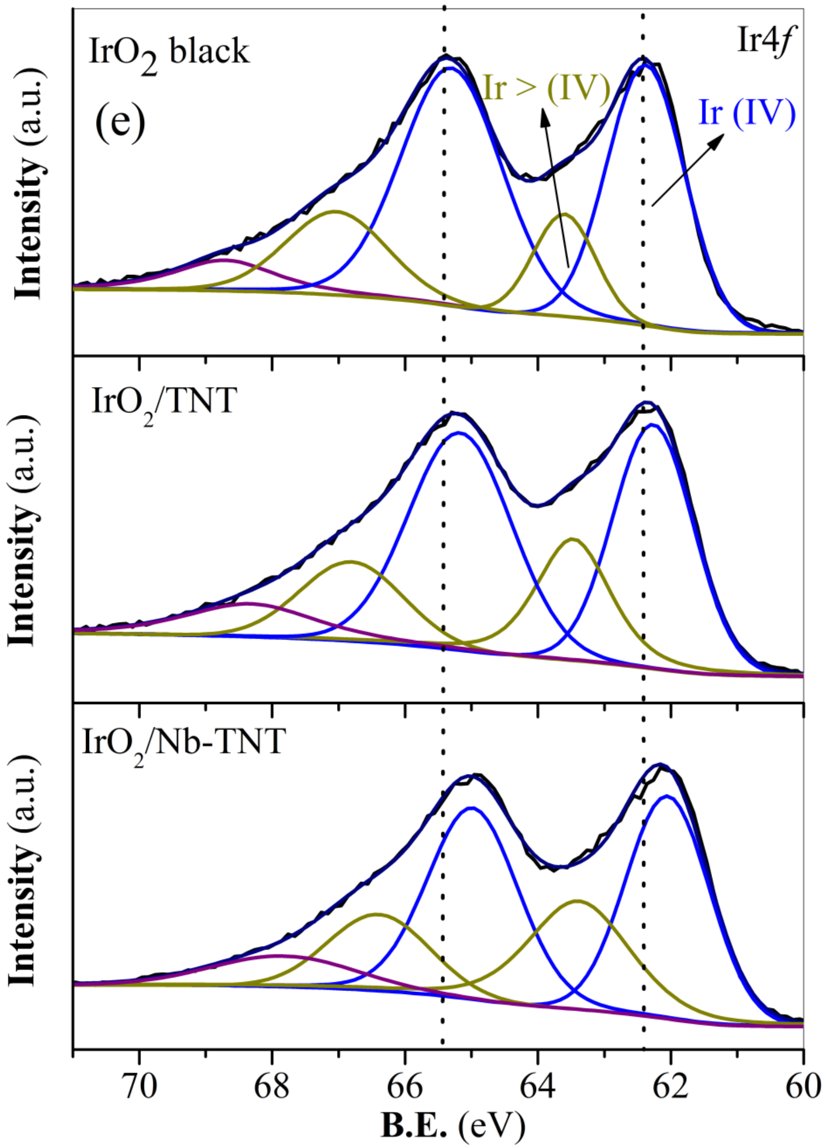

Fig. 3. Deconvoluted high resolution XPS spectra of (a) C 1*s* and Ru 3*d* regions of $IrRuO_x$ and IrO_2 blacks, (b) Ti 2*p* region of IrO_2/TNT and IrO_2/Nb-TNT, (c) Nb 3*d* region of IrO_2/Nb-TNT, (d) Ir 4*f* region of $IrRuO_x$ and IrO_2 blacks, and (e) Ir 4*f* region of IrO_2/TNT, IrO_2/Nb-TNT and IrO_2 black (for comparison).

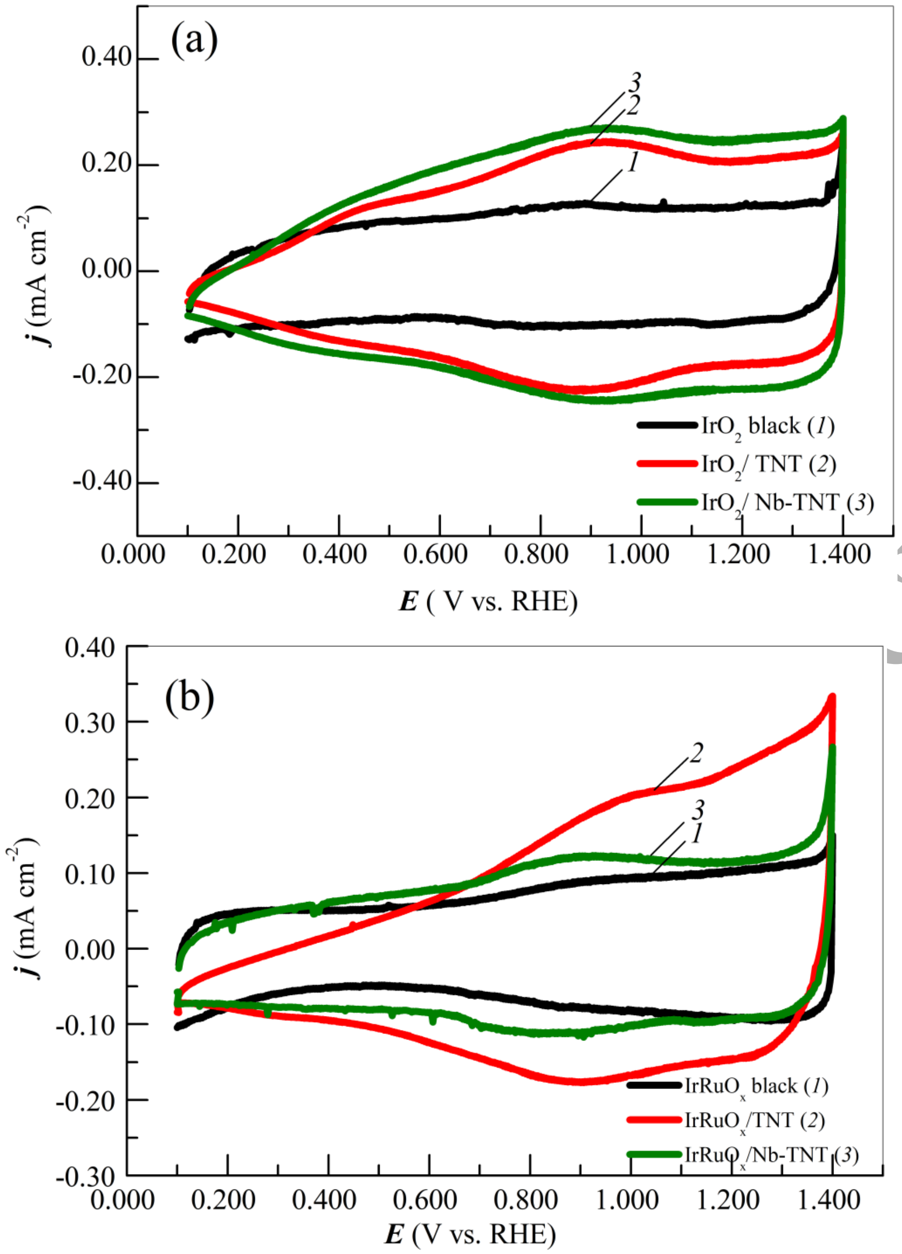

Fig. 4. Cyclic voltammograms in deaerated 0.50 mol dm^{-3} H_2SO_4 for (a) IrO_2 and (b) $IrRuO_x$ based unsupported and supported catalysts registered under 20 mV s^{-1} and $T = 25$ °C.

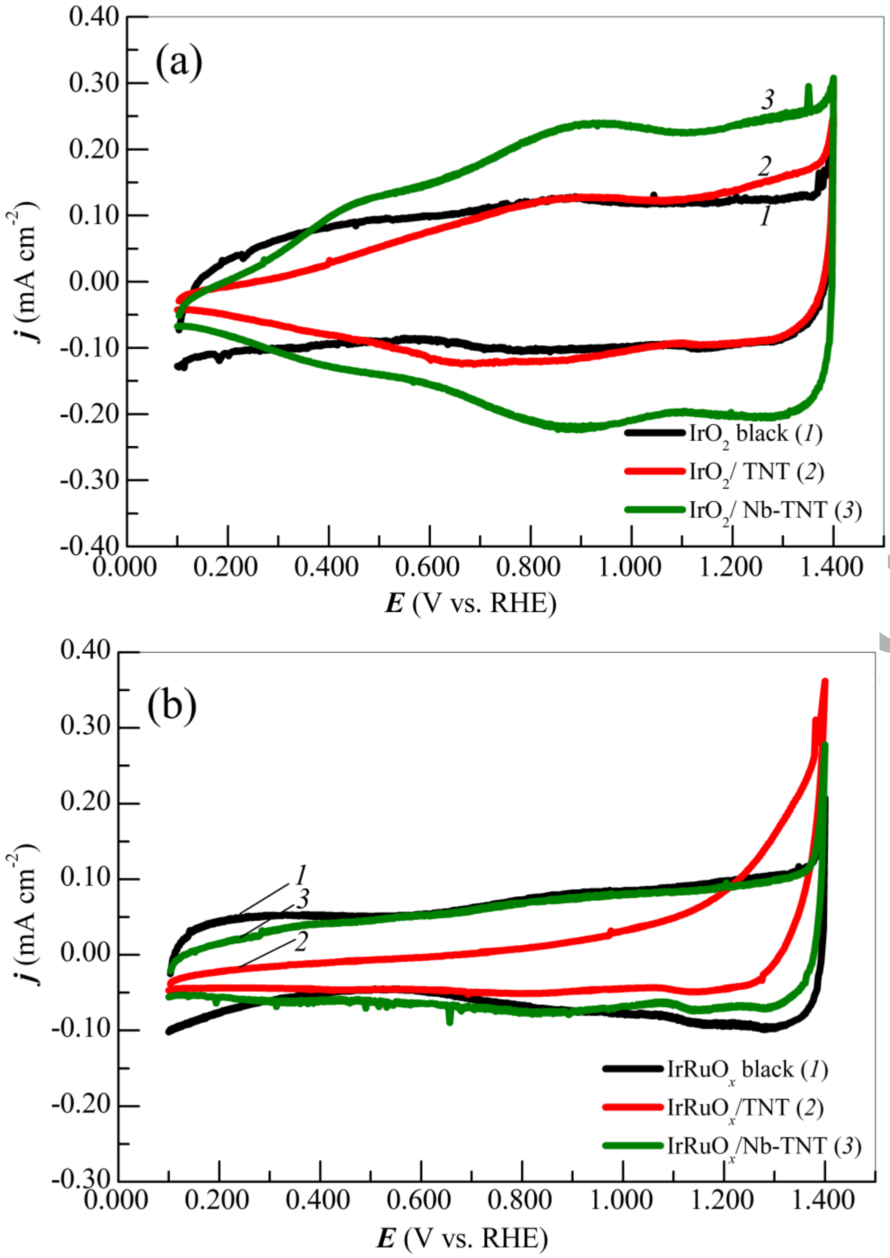

Fig. 5. Cyclic voltammograms in 0.5 mol dm^{-3} H_2SO_4 recorded at 20 mV s^{-1} for the different (a) IrO_2 and (b) $IrRuO_x$ based catalysts, after three consecutive linear sweep voltammograms between 1.2 and 2.0 V at 1 mV s^{-1} (the plotted curves correspond to the fifth cyclic voltammograms). T = 25 °C.

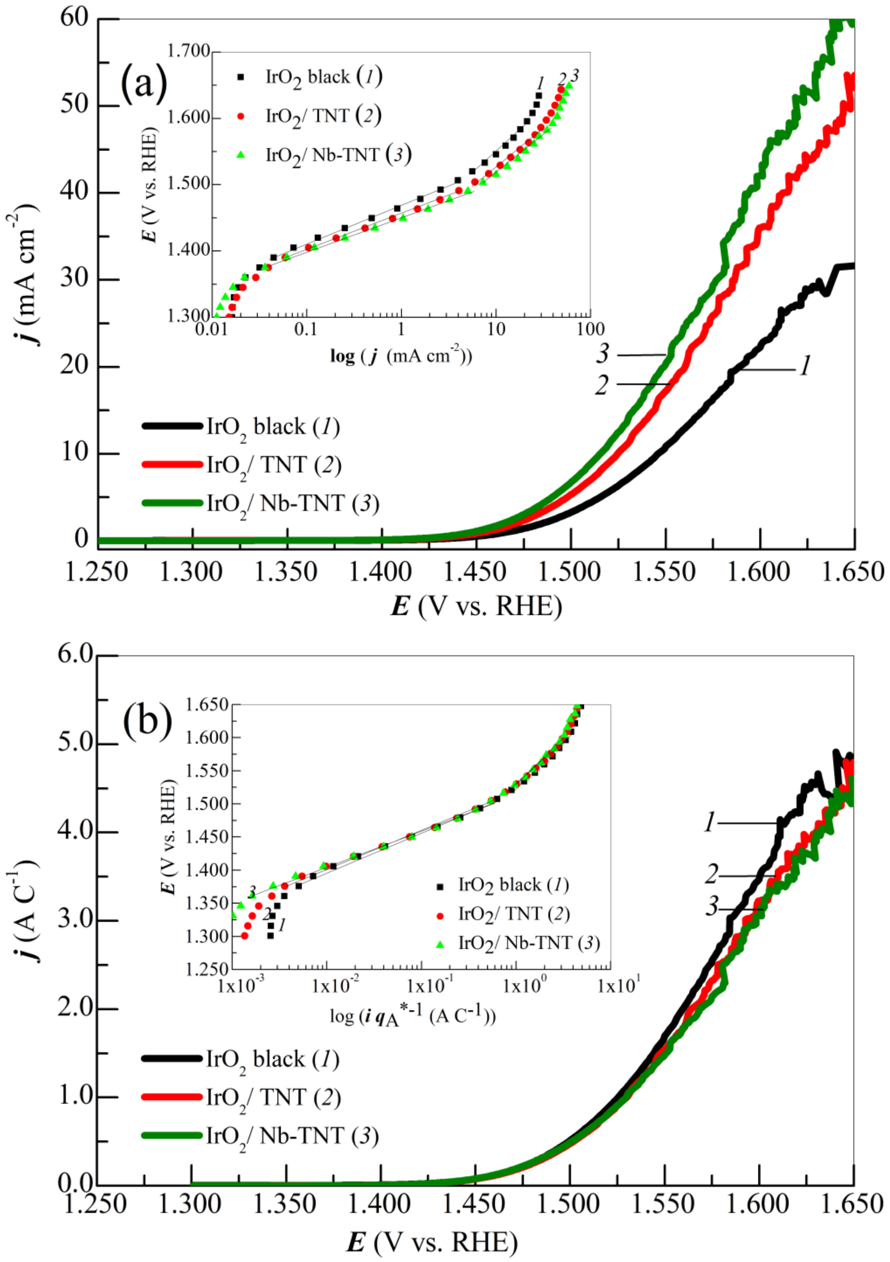

Fig. 6. *j*-*E* curves referred (a) to the electrode section and (b) to the total charge, corresponding to the OER on (1) IrO_2, (2) IrO_2/TNT and (3) IrO_2/Nb-TNT catalysts in 0.50 mol dm^{-3} H_2SO_4 at 1 mV s^{-1}. T = 25 °C. The corresponding Tafel plots are given in the insets. *IR*-drop corrected.

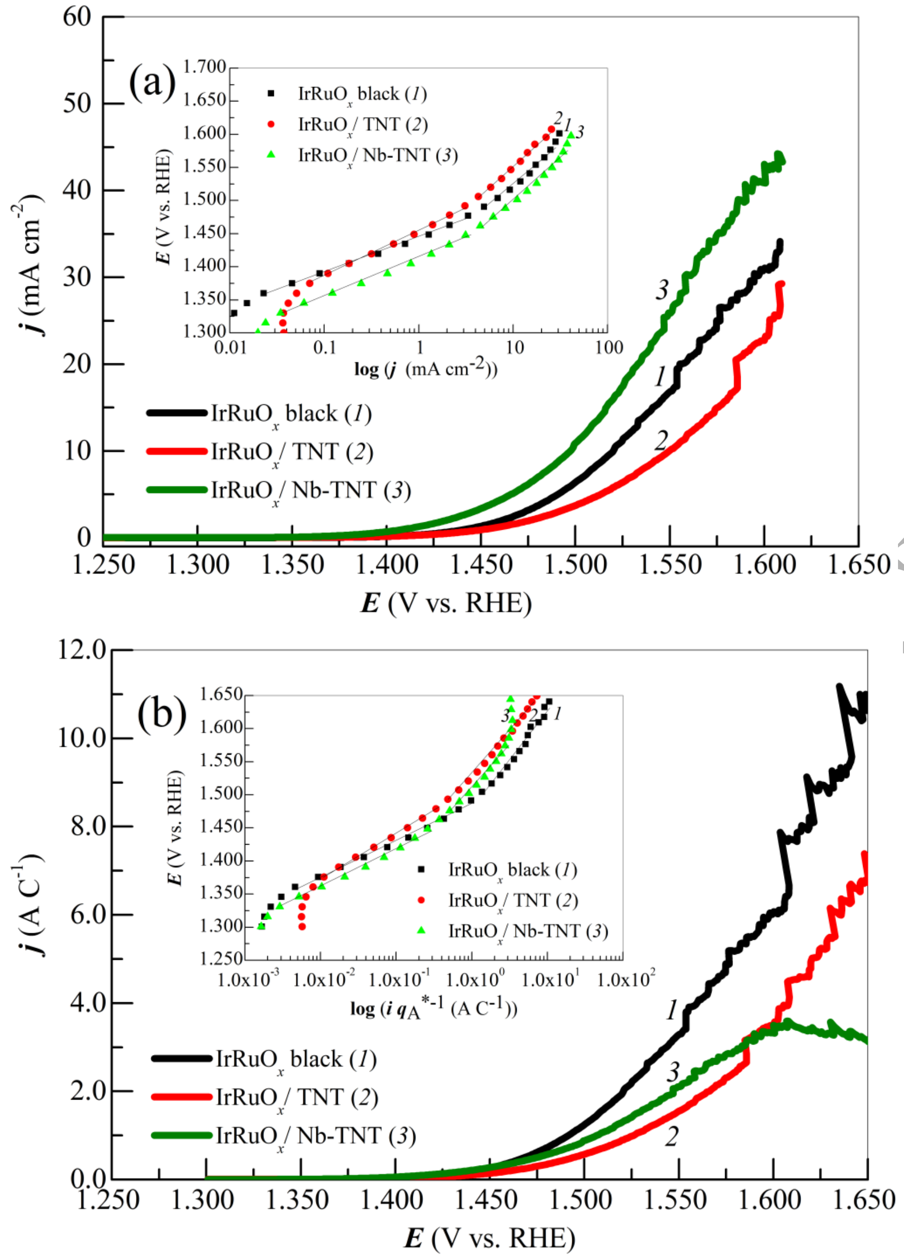

Fig. 7. *j*-*E* curves referred (a) to the electrode section and (b) to the total charge, corresponding to the OER on (1) IrRuO$_x$, (2) IrRuO$_x$/TNT and (3) IrRuO$_x$/Nb-TNT catalysts in 0.50 mol dm^{-3} H$_2$SO$_4$ at 1 mV s^{-1}. *T* = 25 °C. The corresponding Tafel plots are given in the insets. *IR*-drop corrected.

TOC

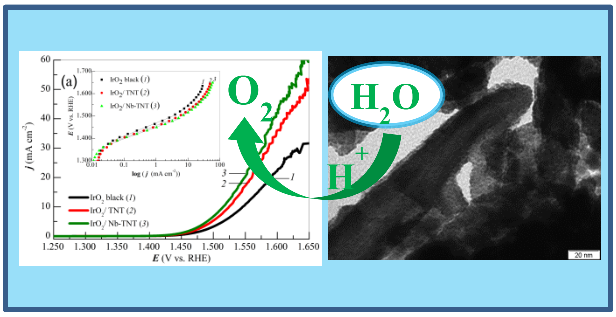

IrO_2 nanoparticles successfully supported on high surface area Nb-doped titanium dioxide nanotubes enhance oxygen evolution in aqueous acidic solution, which makes this catalyst a promising candidate for PEM water electrolyzers.